UNIVERSITY OF OSLO
Department of Geosciences

On the Vertical Partition of Kinetic Energy in the Ocean. A Comparison between Flat and Steep Bottom Modes

Master Thesis in Geosciences Meteorology and Oceanography

Helle Kristine Fuhr

22 June 2015

Abstract

Observational data from 61 moorings was used to decompose vertical velocity fields into its modal components using two different approaches, one assuming a flat bottom ocean and one assuming an ocean with rough topography. Also an analytical solution with idealized stratification was calculated. The modes were compared to the most dominant empirical orthogonal functions (EOFs). To be able to predict the vertical structure of the kinetic energy is of great relevance when interpreting surface velocity fields measured by altimeters. The results show that the most dominant EOF on average accounts for 75% of the variance and resembles the shape of a first baroclinic steep bottom mode. We are able to predict the structure in the pycnocline layer fairly well for the mooring located in the mid-latitudes as long as they are not too close to the coast or in shallow areas. For the high latitudes the picture is more complicated. An analysis of the flat bottom mode is also carried out and gives results in agreement with previous studies finding the barotropic and first baroclinic modes to account for most of the column-averaged kinetic energy. The question remains if we should interpret the dominant EOF as a coupling between the barotropic and first baroclinic mode, or as the first baroclinic steep bottom mode. If the latter is true only one mode is needed for interpreting altimeter data and the dominant elements for the kinetic energy will be the first baroclinic mode, and a bottom trapped topographic wave which is independent and do not have to be correlated to the baroclinic modes.

Acknowledgements

First and foremost I would like to thank my supervisor Joe LaCasce. Thank you for giving me the opportunity to "go up against" Wunsch, one of my favorite oceanographers. It has certainly been challenging, but I have learned a lot. Thank you for sharing your contagious enthusiasm, and for excellent guidance throughout the year. I greatly appreciate that you have always been available to answer my questions, even though you are on your sabbatical.

The extent of this thesis would not have been the same without the kindness of Robert Scott who shared the GMACMD data set with us.

There is a small and exclusive list of academic superheros I would like to thank. First a special thanks to Marta for helping me get started and for all your loving support. A big thank you to Pål Erik for sharing your outstanding MatLab skills and for valuable feedback during the Friday group sessions. I would also like to thank to Lars Petter and Eyvind for always taking the time to answer my wee questions. And last, but not least a great thanks to Ada for convincing me that Oslo is the place to be and for making dynamics so interesting.

This year would not have been the same without Marta and Mari. Thank you for all the encouragement, positivism and for being the best study friends in the world. I am also grateful for the positive learning environment created by all my fellow students at the study hall.

My friends and and family also deserves a thank you for all the encouragement and for trying to understand what I have been wrapping my head around for the past years. Most of all I would like to thank Roar for keeping me sane and for all the care and support throughout.

Contents

List of Figures

Chapter 1

Introduction

"How inappropriate to call this planet Earth when it is clearly Ocean."
-Arthur C. Clarke

70% of the Earth is covered by the ocean. The ocean stores vast amounts of thermal energy and is therefore an important factor for the climate on Earth. The heat is carried from the Equator towards the poles by currents. The currents are either wind driven, or set up by density differences. The wind driven circulation is fairly well understood. Sverdrup [1947] related the curl of the wind stress to the transport in the upper ocean, and Stommel [1948] showed that there is an asymmetry in the ocean gyres resulting in a western boundary current. The two theories combined explains the general picture we see when looking at the World Ocean from above.

In 1992 NASA and the French space agency (CNES) launched the oceanographic satellite TOPEX/ Poseidon, a satellite designed to observe sea surface height (SSH). The mission revolutionized oceanography providing scientists with global coverage of the SSHs every 10 days. 23 years later over 4000 publications from 20 different countries have been related to altimeter data from TOPEX/ Poseidon, and the succeeding satellites Jason 1 and Jason 2 [NASA, n.d.]. The 4^{th} generation oceanographic satellite, Jason 3, is scheduled to be launched 22 July 2015.

The altimeter data together with sea surface temperatures (SSTs) and sea surface salinities (SSSs) from satellite data is used used to e.g. keep track of sea level rise by monitoring the total volume of the ocean, look at seasonal heating and cooling of the ocean, follow how the heat is transported with the circulation patterns and to track ocean eddies [NASA, n.d.]. The forecasting models have also improved after global altimeter data became available. From the altimeter data one can calculate the slope of the sea surface and the surface geostrophic currents can be found. The satellite data is of great value for understanding the ocean surface and its circulations patterns. The interior circulation however, is less documented. Measurements

of the vertical current profile are tedious and expensive. The spatial and temporal coverage of the ocean surface is not achievable for the interior ocean. This has motivated several studies on how to extrapolate the surface geostrophic current to below the surface.

In literature there are two main approaches on how to extrapolate the surface signal below the surface. One method is to use vertical modes. Wunsch [1997] found that much of the World Ocean is dominated by the barotropic and first baroclinic mode. Another result, that has remained a corner stone for interpreting altimeter data, is that the SSH to a first approximation reflects the first baroclinic mode. This is consistent with Wunsch & Stammer [1997] who observed that the length scale of zero crossing of the spatial autocorrelation of the SSH and the first Rossby deformation is proportional. Thus, the first baroclinic mode processes are dominating the observed SSH fluctuations. Scott & Arbic [2007] finds a surface energy budget that is very similar to the first baroclinic mode energy budget, using a two-layered model of quasigeostrophic turbulence. This is supported by Smith & Vallis [2001] who used simulations to look at quasigeostrophic turbulence. When simulating an oceanlike stratification their findings showed that the first baroclinic mode dominates over the barotropic mode contribution to the surface kinetic energy.

The second approach is based on surface quasigeostrophic (SQG) theory. The three-dimensional circulation in the upper ocean is assumed to be in geostrophic balance, and the potential vorticity (PV) in the interior of the fluid is assumed to be zero. The surface boundary is observed from the satellites, via surface temperature anomalies. By matching the surface boundary conditions to a reference solution, an approximation to the 3D circulation is found. The method was explored by Lapeyre & Klein [2006] who used simulations of the Antarctic Circumpolar Current, and LaCasce & Mahadevan [2006] who applied the SQG approximation to *in situ* observations in several regions. Both studies assumed a constant Brunt-Väisälä frequency, and they found that the SQG model gives reasonable results for the qualitative structure of the subsurface flow. However, it consistently underestimated the strength. LaCasce [2012] looked at a modified version of the SQG model with a more realistic stratification where the Brunt-Väisälä frequency was assumed to decay exponentially with depth. This made matters worse weakening the velocities even further.

Scott & Furnival [2012] introduced a modified version of the SQG approach, using a surface boundary condition that matches the SSHs rather than the SSTs. This changed the surface boundary condition from Neumann to Dirichlet. The resulting set of basis functions was compared with the traditional first baroclinc and barotropic mode and a phase locked linear combination of those two modes. They found the new basis functions to preform the best below 1200 m. A combination between the SQG method and the barotropic and first baroclinic modes was investigated by Wang *et al.* [2013]. They used model simulations of the North Atlantic

to test the approach and the subsurface velocity fields and density fields was successfully predicted down to about 1000 m depth.

LaCasce & Wang [2015] (unpublished) are looking into the influence of topography using steep bottom modes with exponential stratification. The anticipation is that the first baroclinic steep bottom mode is sufficient to predict the subsurface flow. In this thesis we are applying this idea to *in situ* observations. We are looking at steep bottom modes using realistic stratification, and compare this to an analytical solution using exponential stratification. We also look at flat bottom modes and compare our results to Wunsch [1997]. EOFs are used to find patterns in the vertical structure, which is compared to the two sets of dynamical modes.

Background theory on ocean stratification and the governing equations is presented in chapter 2. In chapter 3 the reader is introduced to the data sets and methods used for the thesis. Results and discussion are presented in chapter 4 before a summary and some concluding remarks are given in chapter 5.

1.1 Motivation

The ultimate goal is to be able to construct a full three-dimensional wavenumber and frequency spectrum from the sea surface information obtained from satellites. A method that successfully reconstructs the subsurface fields from altimeter data will broaden our understanding of the ocean tremendously. The focus for this thesis will be on the mechanisms that sets the vertical structure in the ocean.

Wunsch [1997], hereafter referred to as W97, used observational data from 103 moorings located mostly in the northern hemisphere and with greatest coverage in the Atlantic ocean to analyze the vertical partition of kinetic energy. The analysis of the vertical structure was done separately for the velocity components in east-west direction, u, and north-south direction, v. The data was filtered to a once per day value,

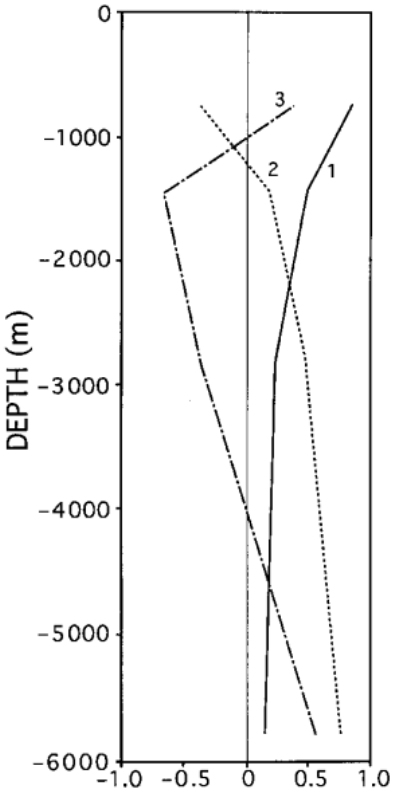

Figure 1.1: Typical EOFs for the horizontal velocity component, 1 being the mode of interest representing the most dominant structure. *Source: Wunsch [1997]*

and the time means were removed. Linear dynamical modes was calculated from annual mean climatology, assuming a flat bottom. The velocities was projected onto the modes using a linear mode fit described in section 3.3. The surface kinetic energy was calculated separately and compared to global surface geostrophic kinetic energy estimated from local slopes of three years of TOPEX/ Poseidon data.

The study concludes that the barotropic and first baroclinic modes are the two dominant ones over much of the World Ocean. This has later been supported by analysis of observations by Argo float data [Cabanes *et al.*, 2008], observations from satellite data [Chelton *et al.*, 2011] and by model simulations [Smith & Vallis, 2001]. The altimeter is, according to W97, to a first approximation reflecting the movement of the thermocline, as the surface kinetic energy is dominated by the first baroclinic mode. Even though there are several limitations pointed out in the study, this result is extensively used in literature. It is argued that the barotropic and first baroclinic modes are canceling each other below the thermocline, and that the barotropic mode is more important below the thermocline. Together the two modes should account for as much as 90% of the water column-average kinetic energies. W97 shows using empirical orthogonal functions (EOFs) (see figure 1.1) that the barotropic and baroclinic modes are the most dominant ones by saying that the most dominant EOF looks like a linear combination of the two modes. We will argue that the dominant function might depict the first baroclinic steep bottom mode.

When using steep bottom modes one is assuming that the flow at the bottom is zero. This changes the bottom boundary condition, forcing the modes to go to zero at the bottom. The barotropic mode vanishes and is replaced by a bottom trapped topographic wave [Pedlosky, 1979]. The first baroclinic mode has no zero crossing. W97 claims that the EOFs in figure 1.1 are typical results both in his investigation and in literature. We see that the structure of function 1 is similar to what we would expect from steep bottom modes. Function 2 could be a topographic wave. The aim of this thesis is to answer if the dominant function from the EOFs should be interpreted as a coupling between the barotropic and first baroclinic mode, or if this simply represents the first baroclinic steep bottom mode.

Chapter 2

The Oceans Vertical Structure

The stratification of the ocean determines the dynamical modes, which tells us something about what the vertical velocity profile look like. In this chapter a brief introduction of ocean stratification is given before the governing equations are introduced. We look at analytical solutions for flat and steep bottom modes assuming both constant and exponential stratification. When using stratification from observations we have to rely on numerical methods to solve the problem. This will be introduced in chapter 3.

2.1 The Density Structure

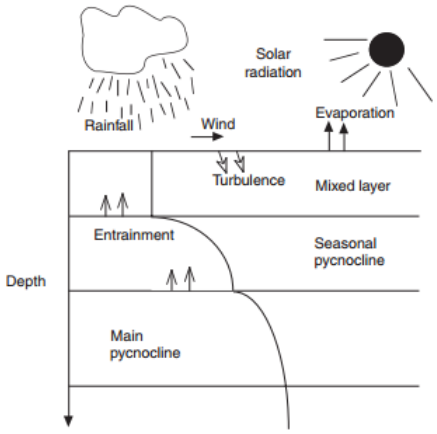

Figure 2.1: Conceptual diagram of the vertical structure of the upper ocean, and the forcing and physics that govern its existence. *Source: Sprintall & Cronin [2001]*

The ocean is divided into layers dependent on the density. The layering of the ocean is called stratification. In reality the ocean is continuously stratified. However, when describing the ocean we often divide into three layers: the mixed layer, the pycnocline layer and the deep layer. At high latitudes, the structure differs from the normal and we do not always see a three layered structure. The depth of the layers are dependent on temperature and salinity, and might change with seasons. The surface of the ocean is heated by the sun and becomes warmer, and hence lighter, than the deep waters. Fresh water input is also contributing to making the upper layers less dense. Gravity separates the layers such that the heavier waters lies below lighter water

[Sprintall & Cronin, 2001].

The density gradient between the surface layer and the deep layer is called the pycnocline. This is the region where the density is increasing rapidly with depth. In most of the ocean the density structure is set by temperature differences, making the pycnocline a thermocline. At high latitudes the salinity is more important than temperature in determining the density, making the pycnocline a halocline. In some areas a seasonal pycnocline can appear due to surface heating from the sun in mid-latitudes, or fresh water input from rainfall, rivers or ice melt in subpolar regions (see figure 2.1). For this thesis, when referring to the pycnocline we mean the permanent pycnocline that is present regardless of season. When talking about the surface layer, we are referring to the layer above the pycnocline.

The pycnocline is important for determining the physical and biological properties in the ocean and the strong density gradient inhibits vertical motion across the pycnocline. The surface layer is influenced by the air-sea exchanges of wind and heat. Turbulent mixing, waves, and strong surface currents are induced. Below the base of the pycnocline the waters has not seen the surface for a long time [Sprintall & Cronin, 2001]. The density increases steadily with depth. Within this deep layer the waters no longer feel the winds at the surface and motion is often slow throughout most of the water column. The velocities can be intensified towards the bottom due to bottom currents or topographic waves.

To understand the property of the pycnocline it is useful to introduce the concept of stability. We consider a water column initially at rest in a constant gravity field. A small parcel is then moved vertically a small distance without altering the background pressure field. If the parcel is lighter than its new surroundings it will accelerate upwards until it reaches waters with the same density. The fluid is then statically unstable with lighter waters above heavier water. If, however, the parcel is heavier than its surroundings the parcel will sink back towards its original position and oscillate around this depth. Such a fluid is statically stable. To help us quantify the stability we use the Brunt-Väisälä frequency, N^2. If $N^2 < 0$ the water column is unsta-

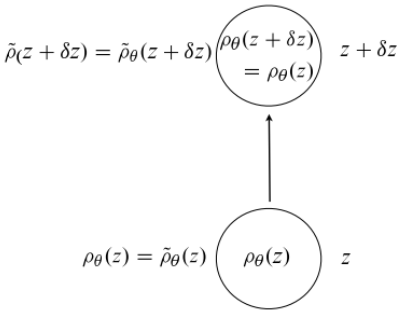

Figure 2.2: A parcel displaced vertically a distance δz without altering the background field. The equations denotes the density of the parcel and the background field respectively. *Source: Vallis [2006]*

ble, if $N^2 = 0$ it is neutrally stable and if $N^2 > 0$ it is stable.

Figure 2.2 shows how this is expressed mathematically. Following Vallis [2006] a parcel is displaced adiabatically a distance δz. The potential density ρ_θ of the parcel is conserved. The parcel is displaced vertically from z to $z + \delta z$. The pressure at $z + \delta z$ is used as the reference level. The difference in density between the parcel and its surroundings is then

$$\delta\rho = \rho_\theta(z + \delta z) - \tilde{\rho}_\theta(z + \delta z) = \rho_\theta(z) - \tilde{\rho}_\theta(z + \delta z) \tag{2.1}$$

$$= \tilde{\rho}_\theta(z) - \tilde{\rho}_\theta(z + \delta z) = -\frac{\partial\tilde{\rho}_\theta}{\partial z}\delta z,$$

where ρ is the *in situ* density of the parcel and the density of the environment is noted with a tilde. The upward force on the parcel we displaced is

$$F = -g\delta\rho = g\frac{\partial\tilde{\rho}_\theta}{\partial z}\delta z. \tag{2.2}$$

Newton's second law gives

$$\frac{\partial^2\delta z}{\partial t^2} = \frac{g}{\rho}\left(\frac{\partial\tilde{\rho}_\theta}{\partial z}\right)\delta z = -N^2\delta z, \tag{2.3}$$

where

$$N^2 = -\frac{g}{\tilde{\rho}_\theta}\frac{\partial\tilde{\rho}_\theta}{\partial z}. \tag{2.4}$$

Density variations in the ocean are usually small compared to the mean density. The Bousinessq approximation is therefore considered to be valid for the ocean, saying that the density is constant except in the buoyancy term. This is the same as saying that we have an incompressible fluid. The Brunt-Väisälä frequency is then approximated to

$$N^2 = -\frac{g}{\rho_c}\frac{\partial\tilde{\rho}_\theta}{\partial z}, \tag{2.5}$$

where ρ_c denotes a constant density. The Brunt-Väisälä frequency is a key factor in determining the shape of the baroclinic modes. In the following section we will introduce the governing equations, ending at the eigenvalue problem giving us the vertical structure in terms of dynamical modes.

2.2 Baroclinic modes

The following theory is based on the books by Pedlosky [1979] and Vallis [2006] and on the compendium "Atmosphere-Ocean dynamics" by LaCasce [2014].

In a barotropic flow the isobars are parallel with the isopycnals resulting in the

same velocity throughout the water column. A baroclinic flow has different speed, and can also change direction throughout the water column. Calculating the dynamical modes says something about the vertical structure of the ocean. The modes originate from the governing equations.

The velocities in the ocean are governed by the momentum equation

$$\frac{D}{Dt}\vec{u} + f\hat{k} \times \vec{u} = -\frac{1}{\rho}\nabla p - g\hat{k} + \vec{F}, \tag{2.6}$$

where the first term on the left hand side $\frac{D}{Dt}\vec{u} = \partial_t + \vec{u} \cdot \nabla\vec{u}$ describes the accelerations and the second term is related to the rotation of the earth and describes the Coriolis force. The first term on the right hand side represent the pressure forcing and the second term is the forcing due to gravity. The last term represent friction. Separating the momentum equation into its components gives

$$\partial_t u + u\partial_x u + v\partial_y u + w\partial_z u - fv = \frac{1}{\rho}\partial_x p + F_x \tag{2.7}$$

$$\partial_t v + u\partial_x v + v\partial_y v + w\partial_z v + fu = \frac{1}{\rho}\partial_y p + F_y \tag{2.8}$$

$$\partial_t w + u\partial_x w + v\partial_y w + w\partial_z w = -\frac{1}{\rho}\partial_z p - g + F_z \tag{2.9}$$

where u, v and w is the velocities in x, y, z direction respectively, f is the Coriolis parameter, ρ is the density, p is the pressure, g is the gravity and F is the friction.

Vorticity is a measure for the rotation of a fluid. Since we are living on a rotating earth we have to consider our equations both in a fixed frame and in a rotational frame. We divide the vorticity into relative vorticity

$$\vec{\zeta} = \nabla \times \vec{u} = (\partial_y w - \partial_z v, \partial_z u - \partial_x w, \partial_x v - \partial_y u) \tag{2.10}$$

and the rotational term, or the planetary vorticity, $2\vec{\Omega}$. Adding the two terms together gives the absolute vorticity

$$\vec{\zeta_a} = \nabla \times (\vec{u} + \vec{\Omega} \times \vec{r}) = \vec{\zeta} + 2\vec{\Omega}. \tag{2.11}$$

By doing a scaling analysis we find that on a synoptic scale the horizontal velocities are much bigger than the vertical velocities, thus the vertical component of the vorticity is the most important

$$\zeta_a \cdot \hat{k} = (\partial_x v - \partial_y u) = 2\Omega \sin(\theta) = \zeta + f, \tag{2.12}$$

where f is the Coriolis parameter. We also assume that friction is small, that the fluid is incompressible (Boussinesq approximation), and we are making use of the β-plane approximation. The momentum equation is then, in x direction reduced to

$$\partial_t u + u\partial_x u + v\partial_y u - fv = \frac{1}{\rho_c}\partial_x p \tag{2.13}$$

and in y direction we have

$$\partial_t v + u\partial_x v + v\partial_y v + fu = \frac{1}{\rho_c}\partial_y p. \tag{2.14}$$

We take the x derivative of 2.14 and subtract the y derivative of 2.13 to get the vorticity equation

$$\frac{D_H}{Dt}(\zeta + f) = -(\zeta + f)(\partial_x u + \partial_y v) = (\zeta + f)\partial_z w \tag{2.15}$$

where $\frac{D_H}{Dt} = \partial_t + u\partial_x + v\partial_y$. By integrating the vorticity equation over depth we can show that for a barotropic fluid, in the absence of friction, the potential vorticity (PV) is conserved. This is also true for a baroclinic fluid by choosing a scalar field that is a function of density and pressure alone. No such restrictions are necessary for a barotropic fluid.

The quasi-geostrophic vorticity equation is commonly used on synoptic scales. A geostrophic current is one where there is a balance between the pressure gradient force and the Coriolis force. The velocity is divided into a geostrophic component and an ageostrophic component

$$\vec{u} = \vec{u_g} + \vec{u_a} \tag{2.16}$$

where we assume that $\vec{u_a} \ll \vec{u_g}$. In other words, we assume that the Rossby number ϵ is small. We also assume that $|\beta y| \ll f$ and that the bottom topography is weak. The streamfunction is defined as

$$\psi = \frac{p}{\rho_c f_0}. \tag{2.17}$$

The velocity and vorticity can then be expressed by

$$u = -\partial_y \psi, \quad v = \partial_x \psi, \quad \zeta_g = \nabla^2 \psi. \tag{2.18}$$

By implementing the streamfunction and the assumptions above the vorticity equation can be expressed by

$$(\partial_t - \partial_y \psi \partial_x + \partial_x \psi \partial_y)(\nabla^2 \psi + f) = f_0 \partial_z w. \tag{2.19}$$

This equation has two unknowns, namely ψ and w. In order to solve the problem for a baroclinic flow where vertical shears are present, we need a second equation.

The density equation is based on the assumption that the vertical velocities are small, which gives a balance between the pressure gradient and the gravity force in the vertical. This is known as hydrostatic balance and is considered to be a good approximation on synoptic scale. The thermodynamic equation for the ocean is

$$\frac{D\rho}{Dt} = \partial_t \rho + \vec{u} \cdot \nabla \rho = 0. \tag{2.20}$$

Since we have assumed hydrostatic balance we can divide the pressure and the density into a stationary background field, and a moving part

$$p = p_0(z) + p(x, y, z, t) \qquad \rho = \rho_0(z) + \rho'(x, y, z, t). \tag{2.21}$$

The background field is assumed to be much larger than the perturbations. Substituting this into the thermodynamic equation and making use of the hydrostatic balance gives the density equation

$$(\partial_t - \partial_y\psi\partial_x + \partial_x\psi\partial_y)\partial_z\psi + \frac{N^2}{f_0}w = 0. \tag{2.22}$$

We have here used the Brunt-Väisälä frequecy N^2 introduced in equation 2.5. In this thesis we will assume a stable stratified ocean, meaning that N^2 is real and positive.

The density equation has two unknowns, ψ and w. Hence, the density equation and the vorticity equation 2.19 can be combined. We first multiply the density equation by f_0^2/N^2 and then take the derivative with respect to z. After some algebra we get the following expression for the density equation

$$(\partial_t + \vec{u}_g \cdot \nabla)[\partial_z(\frac{f_0}{N^2}\partial_z\psi)] = -f_0\partial_z w. \tag{2.23}$$

When we combine this with the vorticity equation, the terms on the right hand side cancels out and we are left with one equation with one unknown

$$(\partial_t + \vec{u}_g \cdot \nabla)[\nabla^2\psi + \partial_z(\frac{f_0^2}{N^2}\partial_z\psi) + \beta y] = 0. \tag{2.24}$$

This equation is known as the quasi-geostrophic vorticity (QGPV) equation. When a fluid is advected by the geostrophic flow the QGPV is conserved. The first term represent the quasi-geostrophic relative velocity, the second term is the stretching vorticity related to the vertical gradients in the density and the third term is the planetary vorticity.

In order to solve for the vertical modes the QGPV equation has to be linearized, assuming constant background flow which gives

$$(\partial_t + U\partial_x)[\nabla^2\psi + \partial_z(\frac{f_0^2}{N^2}\partial_z\psi) + \beta\partial_x\psi] = 0, \tag{2.25}$$

where U is the mean zonal flow. This is a wave equation that can be solved using Fourier transform. The wave solution is then an infinite series of sinusoidal waves. For a linear equation individual wave solutions can be added together to obtain the full solution. Because of the linearity of the equation we can consider the solution for one single wave. The choice of wave solution is dependent on the boundary

conditions.

For this thesis we will assume rigid lid at the surface, $z = 0$. Hence, we assume that the density is constant at the surface boundary. We take the constant to be zero, giving

$$\partial_z \psi = 0, \quad z = 0. \tag{2.26}$$

At the bottom boundary, $z = -H$, we want to look at two different cases. For the flat bottom case we use the same assumption as for the surface, giving

$$\partial_z \psi = 0, \quad z = -H. \tag{2.27}$$

For the steep bottom case we assume that the topography is prohibiting flow at the bottom, so that

$$\psi = 0, z = -H. \tag{2.28}$$

The coefficients in the PV equation are constant with time and in x- and y-direction. Since the Brunt-Väisälä frequency is varying in z-direction an appropriate choice of wave solution will be

$$\psi = Re\{\hat{\psi}(z)e^{i(kx+ly-\omega t}\}. \tag{2.29}$$

Substitution into the linearized QGPV equation gives

$$\partial_z(\frac{f_0^2}{N^2}\partial_z\hat{\psi}) + \lambda^2\hat{\psi} = 0 \tag{2.30}$$

where

$$\lambda^2 \equiv -k^2 - l^2 + \frac{\beta k}{Uk - \omega}. \tag{2.31}$$

This is called the Sturm-Liouville equation and is an eigenvalue problem. Solving for the eigenvalues λ gives us the vertical dynamical modes, which determines the vertical structure, $\hat{\psi}$. The numerical solution to 2.30 is given in section 3.5.

2.2.1 Constant stratification and flat bottom

The solution for a constant N^2, assuming flat bottom, is well know from literature. Following LaCasce [2014] (lecture notes) we have

$$\partial_z^2\hat{\psi} + \frac{N^2\lambda^2}{f_0^2}\hat{\psi} = 0. \tag{2.32}$$

The general solution to this equation is

$$\hat{\psi} = A\cos(\frac{N\lambda z}{f_0}) + B\sin(\frac{N\lambda z}{f_0}) \tag{2.33}$$

where A and B are amplitudes. The upper boundary condition requires $B = 0$. For the lower boundary to be satisfied A either has to equal 0, for which we have no wave, or the following requirement has to be met

$$\sin \frac{N\lambda H}{f_0} = 0. \tag{2.34}$$

This is true when

$$\frac{N\lambda H}{f_0} = n\pi \tag{2.35}$$

for $n = 0, 1, 2....$ The vertical structure is then given by

$$\psi = A\cos(kx + ly - \omega_n t)\cos\frac{n\pi z}{H}. \tag{2.36}$$

If $n = 0$ we get a wave that is constant in the vertical. This is the barotropic mode. If $n = 1$ the streamfunction is a cosine function that has one single zero crossing, hence, is changing sign in the vertical. This is the first baroclinic mode. Figure 2.3a shows the four first baroclinic modes with constant stratification. We see that the modes are symmetrical so that the amplitude at the surface has the same magnitude as the amplitude at the bottom.

The density perturbation associated with the first baroclinic wave is largest in the point where the horizontal velocities disappears. In our solution we have assumed a rigid lid. If we however had allowed the surface to move up and down we would have found a surface deviation with opposite sign to the maximum density perturbation. The surface rises when density contours are pressed down.

2.2.2 Steep bottom modes

For the steep bottom modes the bottom boundary condition is changed forcing the velocities to be zero at the bottom of the ocean. For a constant N we must have

$$\cos \frac{N\lambda H}{f_0} = 0 \tag{2.37}$$

for the boundary conditions to be satisfied. This is true when

$$\frac{N\lambda H}{f_0} = \frac{\pi}{2} + n\pi \tag{2.38}$$

for $n = 0, 1, 2....$ The vertical structure is now given by

$$\psi = A\cos(kx + ly - \omega_n t)\cos\frac{\pi/2 + n\pi z}{H}. \tag{2.39}$$

We no longer have a depth independent contribution, hence the barotropic mode has vanished. The baroclinic modes have one less zero crossing than flat bottom modes, and they show no flow at the bottom. The four first steep bottom modes are given in figure 2.3b. Flows close to the bottom of the ocean are now considered to be bottom trapped topographic waves [Pedlosky, 1979]. Such waves are not orthogonal to the dynamical modes. The waves will influence the depth profile of the currents, but the motion is independent of that set up by dynamical modes.

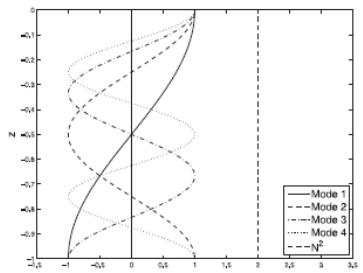

(a) Flat bottom, constant N

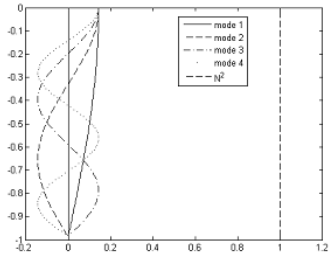

(b) Steep bottom, constant N

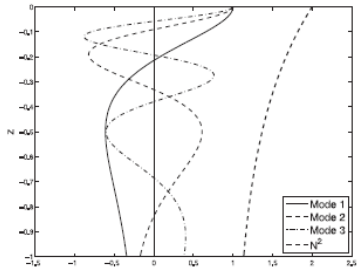

(c) Flat bottom, exponential N ($\alpha = 2/H$)

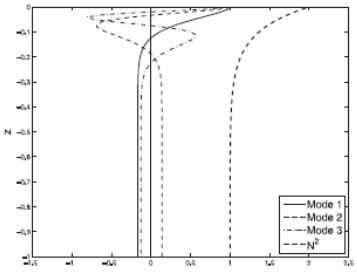

(d) Flat bottom, exponential N ($\alpha = 10/H$)

Figure 2.3: Baroclinic modes. Figure adapted from LaCasce [2012]

Topographic waves

A sloping bottom can induce topographic waves due to conservation of potential vorticity. The waves are propagating with the shallow waters to the right. To examine the structure of the topographic wave we use the linearized QGPV equation 2.25, assuming zero mean flow and $\beta = 0$. For simplicity we assume that N^2 is constant. This gives

$$\partial_t(\nabla^2\psi + \frac{f_0^2}{N^2}\partial_z^2\psi) = 0 \tag{2.40}$$

Following LaCasce [2014] we consider topography in it simplest form; a linear slope with depth decreasing towards the north.

$$h = \alpha y \tag{2.41}$$

The bottom boundary condition is now

$$\frac{d_g}{dt}\partial_z\psi + \frac{N^2}{f_0 t}\alpha v = 0 \tag{2.42}$$

The boundary at the surface is not important for this problem as the wave will be trapped near the bottom. We assume a plane-wave solution for the potential vorticity equation

$$\psi = Re\{\hat{\psi}(z)e^{i(kx+ly-\omega t)}\} \tag{2.43}$$

Substitution into 2.45 gives

$$\partial_z^2 \hat{\psi} - \frac{N^2 \kappa^2}{f_0^2} \hat{\psi} = 0 \tag{2.44}$$

where $\kappa = (k^2 + l^2)^{1/2}$ is the total wavenumber. The solutions to this equation are exponential. We are interested in the one that is decaying going up into the interior of the water column. The vertical structure is then given by

$$\hat{\psi} = Ae^{-N\kappa z/|f_0|}. \tag{2.45}$$

The e-folding scale is

$$H \propto \frac{|f_0^2|}{N\kappa} = \frac{|f_0|\lambda}{2\pi N} \tag{2.46}$$

where λ is the wavelength. This tell us that the larger the waves the further up into the water column they are felt. If we have weak stratification and large waves the topographic wave could be felt all the way up to the surface. This would give a barotropic response analogous to the barotropic mode, though not orthogonal to the barotropic modes.

2.2.3 Exponential stratification

A better approximation to the Brunt-Väisälä frequency is that of an exponential stratification. LaCasce [2012] examined two cases of exponential stratification; one with a vertical decay rate $\alpha = 2/H$ and a steeper one with $\alpha = 10/H$. H denotes the total depth. The density profile was described by

$$N^2 = N_0^2 e^{\alpha z}. \tag{2.47}$$

Substitution into 2.30 gives

$$\frac{d^2\psi}{dz^2} - \alpha \frac{d\psi}{dz} + \frac{N_0^2 \lambda^2}{f_0^2} e^{\alpha z} \psi = 0. \tag{2.48}$$

By making the substitution $\xi = e^{\alpha z/2}$, we get

$$\xi^2 \frac{d^2\psi}{d\xi^2} - \xi \frac{d\psi}{d\xi} + \frac{4N_0^2 \lambda^2}{\alpha^2 f_0^2} \xi^2 \psi = 0 \tag{2.49}$$

which is a Bessel-type equation. Imposing the boundary condition for the surface gives the solution

$$\psi = Ae^{\alpha z/2}[Y_0(2\gamma)J_1(2\gamma e^{-\alpha z/2}) - J_0(2\gamma)Y_1(2\gamma e^{\alpha z/2}], \tag{2.50}$$

where $\gamma = N_0\lambda/(\alpha f_0)$, J_n is Bessel functions of the first kind and Y_n is Bessel functions of second the kind (see figure 2.4. Imposing the flat bottom boundary gives

$$J_0(2\gamma)Y_0(2\gamma e^{-\alpha H/2}) - Y_0(2\gamma)J_0(2\gamma e^{-\alpha H/2}) = 0. \tag{2.51}$$

We can only get solutions for discrete values, γ_n. Also for this case we get a barotropic solution when $\gamma = 0$. Solution for the three first baroclinic modes for two different cases of exponential stratification is given in figure 2.3c-2.3d. The number of zero crossings are increasing with mode number. The amplitudes are no longer symmetrical, but largest at the surface.

Let us consider a different boundary condition for the lower boundary. Following LaCasce & Wang [2015] we let the velocity go to zero as the depths goes to infinity:

$$\vec{v} \to 0, \qquad z \to -\infty. \tag{2.52}$$

The velocities will then vanish with increasing depth and the solution is independent of the sea floor slope. The solution which decays with depth is now on the from

$$F_n \propto e^{\alpha z/2} J_1\left(\frac{2N_0}{\alpha f_0 R_n} e^{\alpha z/2}\right), \tag{2.53}$$

where F_n is the new set of baroclinic modes and we have made used of the baroclinic Rossby radius $R_n = 1/\lambda$. Imposing the surface boundary condition gives

$$J_0\left(\frac{2N_0}{\alpha f_0 R_n}\right) = 0. \tag{2.54}$$

Figure 2.4 shows that the first value where J_0 crosses zero is 2.4048. That gives a Rossby radius

$$R_1 = \frac{N_0}{\alpha f_0 1.2024}. \tag{2.55}$$

We then have an analytical solution to the vertical structure of the first baroclinic mode:

$$F_1 = A e^{\alpha z/2} J_1(2.4048 e^{\alpha z/2}). \tag{2.56}$$

Because of the lower boundary condition the equation was solved without a tran-

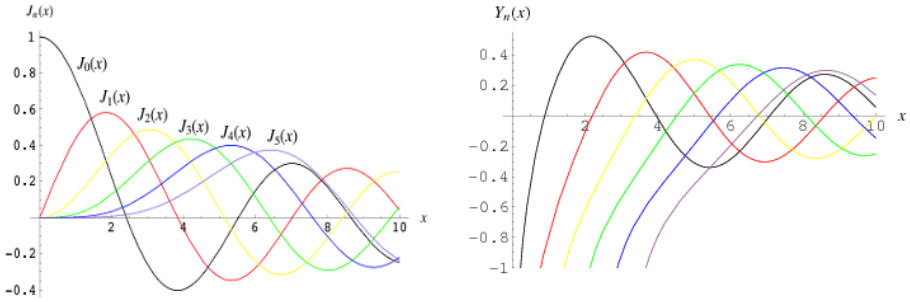

(a) Bessel functions of the first kind (b) Bessel functions of the second kind

Figure 2.4: Bessel functions. *Source: MathWorld–A Wolfram Web Resource [Weisstein, n.d.]*

scendental equation. When imposing boundary condition 2.52 the Y_1 term in equation 2.50 is dropped as it grows with depth. $Y_0(2\gamma)$ is a constant value which we lump into A, leaving us with equation 2.56.

2.2.4 Realistic stratification

For this thesis we are interested in finding which of the two sets of modes mentioned above that best represents the column averaged kinetic energy of the water column. To do this we calculate the modes with realistic stratification and project the velocity profile onto the modes. This has to be done numerically, and the finite difference approximation and methods used are presented in chapter 3.

Chapter 3

Data and Methods

3.1 The Datasets

For the analysis on partition of energy into dynamical modes and the modal fitting described in section 3.5 we use current meter mooring observations. It is strongly preferred that the data sets used are meeting the following requirements [Wunsch, 1997]:

- The instruments have to straddle the main pycnocline
- There should be an instrument in the upper 100 m of the water column
- There should be 6 or more instruments
- The duration should exceed two years
- The depth at the mooring location should be at least 4000 m

For this study we are looking at an alternative method to the flat bottom modes studied by Wunsch, that is steep bottom modes, for which the last requirement can be relaxed. The list of moorings fulfilling all of the conditions listed above are few to none. To get a fair amount of moorings to analyze, it is chosen to relax the number of instruments needed to 4, and the duration to only a 100 days. It is important to remember the limitations of this study introduced by not having longer time series.

The records are obtained from the Global Multi-Archive Current Meter Database (GMACMD) which Robert B Scott kindly has shared with us through personal communication. The GMACMD has an emphasis on current meters and do not have hydrography for all locations used for the thesis. For consistency the background stratification is calculated using temperature and salinity data from the World Ocean Atlas 2009 (WOA09).

World Ocean Atlas 2009

The WOA09 provides objectively analyzed climatology fields of *in situ* salinity and temperature on a 1 degree grid. The analysis is based on historical data and is an average of 5 decadal climatologies. The standard depth for the monthly fields ranges down to 1500 m depth, whilst the annual field has standard depths ranging down to 5500 m. For this thesis we want to be consistent with Wunsch [1997] and are therefore using the annual data set. Seasonal variations in the background stratification is thus not counted for. Down to 1500 meter the annual analysis is defined as the average of twelve monthly mean fields, and below 1500 m the analysis is defined as the mean of 4 seasonal fields. For more information see publications for each of the WOA09 variables, tempereture [Locarnini *et al.*, 2010] and salinity [Antonov *et al.*, 2010]. The dataset is available from the National Centers for Environmental Information [NOAA, n.d.].

GMACMD

The GMACMD is an archive of physical oceanographic time series. Data is collected from several sources and stored with a common format. The archive is readily set up by running a couple of Matlab routines. The scripts run several compile functions, generate time series in .mat format and organize the data into sub archives based on the various sources from where the data was obtained. Both compile routines and original data is easily accessed, and a large collection of functions that serve as analyzing tools are included in the archive.

The sub archives used for this thesis are:

- OSU (from Oregon State University Buoy Group's Deep Water)
- Wunsch 1997 (from Carl Wunsch)
- ZANTOPP (from Rainer Zantopp)
- NODC (from the United States National Oceanographic Data Center, now NOAA)
- IFREMER (from the French Research Institute for Exploitation of the Sea)
- CSIRO (from the Australian Commonwealth Scientific and Research Organization)

To find data that served to our purpose proved to be more difficult than expected. The archive contains data from more than 3000 moorings, and only 61 fulfilled our requirements for the modal fitting. The locations of the moorings used are shown in figure 3.1. The map also shows the surface potential density calculated form the climatological fields of temperature and salinity.

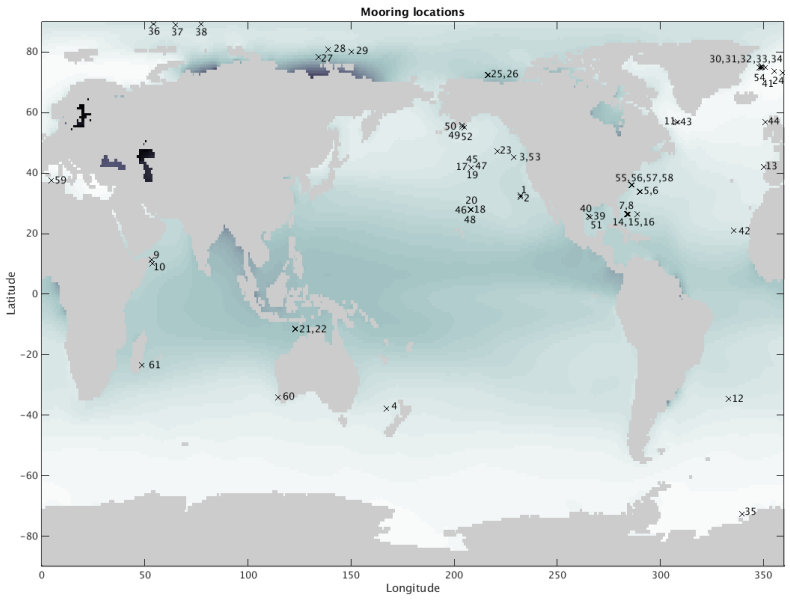

Figure 3.1: A map with the location of the moorings used and their given mooring numbers.

The variables of interest obtained from the GMACMD are mainly the east-west component, u, and the north-south component, v, of the velocity. The standard measuring interval is originally 10 minutes. To remove major tidal effects the time series are filtered to daily averages using one of the accompanying functions. In addition the archive provides us with useful descriptive variables such as latitude, longitude, duration, begin-/end time, instrument depths and sea floor depth. Mooring information and the source from where the data was obtained is also included.

3.1.1 Data Processing Routines

The observational data from the GMACMD is not only obtained from several different sources, but also varies in time by decades. A variety of instruments are used and observing practice might differ. This diversity might have an influence on the quality, accuracy, representativeness and precision of the data used. Limitations introduced by the instruments are discussed in section 3.2.1. To ensure that the time series used do not have any suspect values we ran a set of quality checks provided by the GMACMD archive. The quality check routines relevant for this thesis are presented below. We also removed spikes. For more information about the GMACMD archive or the data processing routines, see Scott & Furnival [2013].

Sea floor depth vs. bottom topography

The sea floor depth from the moorings was compared to a bottom topography file. The sea floor topography used, SRTM30 PLUS v7.0, is on a 30 minutes (about 1 km) grid. The tolerance, tol_1, was set to 1 m and h_{rms} is a measure of the bottom roughness.

$$|\textit{sea floor depth - topography depth}| < tol_1 \cdot h_{rms}. \tag{3.1}$$

Velocity components vs. speed

The velocity components u and v have to be consistent with the speed time series. The tolerance was set to 0.005 for the magnitude and 0.001 for the standard deviation.

$$\max_j |s_j - \sqrt{u_j + v_j}| < tol_2, \tag{3.2}$$

where s_j are elements of the speed time series, u_j are elements of the zonal velocity time series, and v_j are elements of the meridional velocity time series.

Velocity components vs. direction

The direction computed from u and v was compared against the direction time series. If α_j is the elements from the direction time series and β_j is the directions computed from the velocity components, where $j = 1, ..., n$, then

$$\delta_j = |\alpha_j - \beta_j|, \tag{3.3}$$

$$e_j = \begin{cases} 1 & \delta_j < tol_3^* \\ 0 & \delta_j \leq tol_3^* \end{cases}$$

$$\frac{1}{n}\sum_{j=1}^{n} e_j < tol_3 \tag{3.4}$$

where $tol_3^* = 2$ degrees. $tol_3 = 0.1$ is the fraction of time series points that must have a direction error for the warning to be produces.

Removal of Data Spikes

To remove spikes all values were removed (set to NaN) from the time series if they fail to satisfy

$$\overline{x} - C \cdot std(x) < x_i < \overline{x} + C \cdot std(x), \tag{3.5}$$

where C is a constant set to a value of 5, and $\overline{x}$ is the mean of the time series.

3.2 Instruments

The information in this section is based on the books by Emery & Thomson [1998] and Joseph [2014].

Moorings allow scientists to obtain longer time series of oceanographic measurements. A mooring consist of a long cable with an anchor at the bottom end and a float at the other end. The float keeps the cable vertical and can either float at the surface, or be a subsurface float. Measuring devises such as current meters, temperature sensors and salinity sensors are attached to the mooring cable.

The data used for this thesis are, as mentioned above, collected from different sources. The number of instruments used and the distribution throughout the water column therefor vary. When using current meters the question of optimum spacing is always an issue. Instruments are expensive and to cover as much of the water column as possible one would want to have the instruments as far apart as possible. At the same time it is often preferred to have the instruments close enough to each other so that adjacent observations can be correlated. The spacing and number of instruments has to be chosen based on the purpose of the project. The acoustic profiling instruments is nowadays preferred above current meters as one instrument can measure currents in several depths. The current time series used in this thesis have been measured with a variety of instruments. The different current meters used will be briefly introduced, and a list of instruments deployed at the different moorings can be found in the appendix.

3.2.1 Mechanical sensors

All current measuring devices used are Eulerian. This means that the current meter is fixed to a geographic position, measuring the flow of water passing this point. In order to do analysis of the modes, a vertical velocity profile has to be known. To get measurements in several layers a chain of current meters has to be used.

RCM4/5

The Aanderaa rotor current meter, RMC4, and its deep counterpart, RCM5, uses a Savonius rotor to measure the current speed. A Savonius rotor consists of six axisymmetric, curved blades orientated so that they are normal to the direction of the flow. The speed is obtained from the average number of rotor revolutions during a sample period. To find the direction the current meter is equipped with a vane and a tail fin. The instrument is forced to rotate in tune with the current direction. A magnetic compass finds the orientation of the instruments relative to Earth's magnetic north, and hence the direction of the flow.

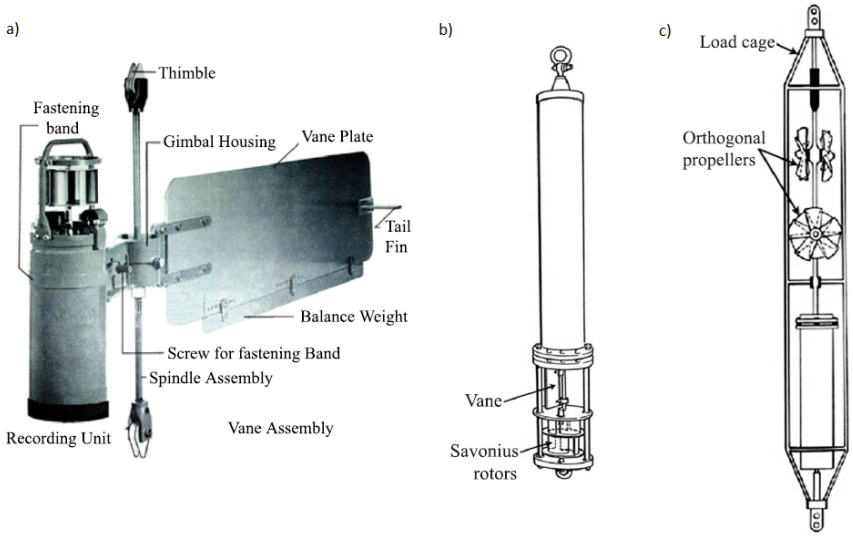

Figure 3.2: The mechanical instruments used in this thesis. a) The rotor current meter (RCM4) coupled to a tailfin. *Source: Aanderaa Instruments Model 4 Current Meter Manual.* b) The vector-averaging current meter (VACM). *Source: Beardsley [1987]* c) The vector measuring current meter (VMCM). *Source: Weller & Davis [1980]*

VACM

The vector averaging current meter (VACM) has proved to perform considerably better in nonsteady flows and was therefore incorporated in the second generation of Aanderaa rotor current meter, RCM7/8. Also this type of current meters uses a Savonius rotor to measure the speed. To indicate flow direction a miniature vane is used. The direction of the vane is recorded relative to the "zero" of the magnetic compass. From the compass and vane output the cosine and sine of the flow relative to Earth's magnetic north is calculated. From this the east-west and north-south direction is found. Calculations are done at each rotor count. After a selected sample interval the vector-averaged mean of registers are stored.

VMCM

The vector measuring current meter (VMCM) is often used in combination with other type of current meters. The instrument is preforming well in near-surface conditions. Two propellers are oriented so that they only respond to flow parallel to their axis of rotation. A compass senses the orientation of the instrument relative to the magnetic north, and the north-south and east-west velocity components are computed and averaged. The speed of the flow is calculated from the revolution rate of the propellers.

Limitations

One problematic issue when deploying instruments on a mooring is vertical displacements. In the presence of strong currents the instruments can be deflected vertically by several meters. The results during such events are biased as the instrument depth does not correspond to the actual depth. One should be aware that in highly energetic regions the results might be distorted.

A major disadvantage with instruments using Savonius rotors (RCM4/5 and VACM) is the contamination of the rotor speed. When there is wave action the mooring moves up and down which can cause "rotor pumping" or over-speeding. The rotor has an ability to accelerate about three times faster than it decelerates, causing an overestimate of the measured velocities. Another problem is the lag in response related to the direction vane. The lag, together with the rotor pumping makes the instruments unsuitable for the upper ocean where there is a lot of waves, and the mean current is small relative to the fluctuations. Bearing friction is also a common problem to all Savonius rotors. The friction results in a relatively high threshold for response. For the RCM4/5 the threshold is about 2 cm/s. That means that there can be currents present that are too slow to be measured.

The VMCMs, with their open fan-type rotors (see figure 3.2) are easily affected by fouling. Small fragments of unwanted material can freely flow into the rotors and influence the measurements. There has been reported cases of small underestimations of the velocities, but compared to the over-registration of velocities of the Savonius rotor the error is small. The sensor threshold is about 1 cm/s.

3.2.2 Nonmechanical sensors

The mechanical sensors limitations when it comes to small structures, rapid changes and weak/ strong currents has motivated the development of the nonmechanical sensors. Highly sensitive sensors were developed using electromechanical, acoustic, laser and thermal technology. In this study data from acoustic Doppler current profiler (ADCP) instruments are used.

ADCP

The ADCP is a profiling instrument taking advantage of the fact that seawater is almost transparent to acoustic radiation. The technology used makes it possible for the instrument to register velocities at a remote distance. The instrument can be both bottom-mounted, sending signals upwards, or mounted close to the surface, sending signals down the water column.

Figure 3.3 shows a schematics of the Doppler effect used to determine the velocity and direction of the water column. The ADCP transmits pulses of sound waves at a constant frequency into the water column. The waves are reflected back when they

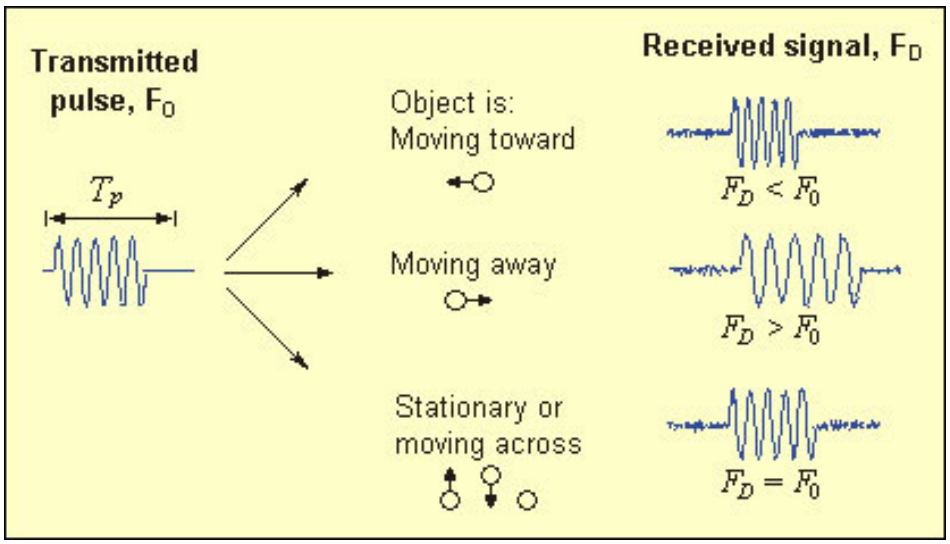

Figure 3.3: A schematic of the transmitted pulse from an ADCP and the received signal and the change in frequency between the two after interaction with an object. (*Source: Sontec*)

hit suspended particles in the moving water. Particles moving towards the instrument will reflect waves of higher frequency and particles moving away will reflect waves of lower frequency. If the particles are stationary or moving across the transmitted signal, the frequency will not change. The difference in frequency between the transmitted signal and the signal received is called the Doppler shift. From this shift the velocity of the particle, and hence the water flow, can be calculated. The traveling time gives the depth from where the signal was reflected. The instrument is equipped with a tilt sensor and a compass. Signals are sent out in four directions. An average of the two horizontal current components over the measure interval is calculated. The direction is found from the tilt and converted to Earth coordinates with help from the compass. The measurements are organized into vertical bins, where the velocities are triangular-weighted averaged over the bin length selected.

There are several advantages using ADCPs over mechanical sensors. First the ADCPs are making remote measurement, so the flow is not influenced by the instrument in any way. The instrument is free from friction, and hence the threshold found in mechanical sensors is not an issue. Weak currents can therefore be measured more accurately. One limitation of the ADCP is that the result is strongly dependent on the assemblage of "drifters" in the water column that can reflect the acoustic signal. Very clear waters can be a problem, and swimming drifters and bubbles can lead to miscalculations.

3.3 Wunsch 1997, Linear mode fit

Wunsch uses data from 103 moorings, located mostly in the northern hemisphere and with greatest coverage in the Atlantic ocean. The data is inhomogeneous in both vertical and temporal coverage. Because of this the method used for modal fitting is based on an a priori statistical hypothesis. It is assumed that the partition of the kinetic energy is in the ration 1:1:1/2:1/4:1/8 for the barotropic through fourth baroclinic modes. To calculate the modal coefficients Wunsch is using the Gauss-Markov estimate

$$\bar{\boldsymbol{\alpha}}_u(t) = \boldsymbol{P}_u(0)\boldsymbol{A}^{\boldsymbol{T}}\boldsymbol{A}\boldsymbol{P}_u(0)\boldsymbol{A}^{\boldsymbol{T}} + \boldsymbol{\sigma}_n^2\boldsymbol{I})^{-1}\boldsymbol{U}(t), \tag{3.6}$$

where $\boldsymbol{U}(t)$ is a matrix of the velocity component, σ_n^2 is an estimate of the observational noise of current meters and $\boldsymbol{A}$ is a matrix with the barotropic through fourth baroclinic mode. $\boldsymbol{P}_u(0)$ is a diagonal matrix

$$\boldsymbol{P}_u = \langle \bar{\boldsymbol{\alpha}}_u(t)\bar{\boldsymbol{\alpha}}_u(t)^{\mathrm{T}} \rangle \equiv \mathrm{E}_u^2 \mathrm{diag}([1 \quad 1 \quad 1/2 \quad 1/4 \quad 1/8])/2.88, \tag{3.7}$$

where E_u^2 is an estimate of the total energy calculated from $\boldsymbol{U}$. 2.88 is the sum of a priori weights. This method produces a minimum variance estimate based on the above-mentioned statistics. A similar calculation is made for $\bar{\boldsymbol{\alpha}}_v$.

The a priori assumption of the partition of the energy ought to effect the results. No such assumptions are used for this thesis, thus we do not consider the inhomogeneous vertical and temporal coverage. One should be careful drawing conclusions from such a coarse coverage as this study provides. However, it is shown that the method used produces much of the same results as Wunsch found. Namely that the barotropic and first baroclinic modes dominate the water-column average kinetic energies. Hence, we consider the results as reliable within their constraints.

3.4 The numerical solution

We want to solve the eigenvalue problem 2.30 with realistic stratification. We use the climatological fields of temperature and salinity to calculate the potential density from which the Brunt-Väisälä frequency, N^2, is found. The climatology is using an unevenly spaced vertical grid of 33 standard depths. We give this grid the name $Z_{standard}$. N^2 is calculated on the mid depths of $Z_{standard}$, and we call this grid Z_{N2}. As the climatological data is available on a 1 degree grid, the calculated N^2 has to be interpolated to the mooring location with latitudes and longitudes given by the GMACMD. A function written by Pål Erik Isachsen is used to calculate the vertical baroclinic modes with the assumption of a flat bottom ocean at rest. The function takes the Brunt-Väisälä frequency profile, the corresponding depth vector (Z_{N2}), the Coriolis parameter and the sea floor depth as inputs. The horizontal velocity structure (the baroclinic modes) and an array with corresponding depths are given as outputs. The modes are calculated on the mid depths of

Z_{N2}, lets call this grid Z_{modes}.

We want to solve the equation

$$A\vec{\psi} = \lambda\vec{\psi} \tag{3.8}$$

where A is an $n \times n$ matrix and λ is the eigenvalue of A with the corresponding eigenfunctions $\vec{\psi}$. The coefficients of the A matrix is found from the stretching operator Γ, which is define as

$$\Gamma \equiv \frac{d}{dz}(\frac{f^2}{N^2}\frac{d}{dz}). \tag{3.9}$$

The finite difference approximation used is adapted from Smith [2007]. A staggered grid is used where N^2 lies one grid and ψ lies on a grid that is staggered half a grid step. The staggered grid gives

$$A = \Gamma\psi = \begin{cases} \frac{f^2}{\Delta z_1}(\frac{-\psi_1+\psi_2}{N_n^2\Delta zm_n}), & n = 1 \\ -\frac{f^2}{\Delta z_n}(\frac{\psi_{n-1}-\psi_n}{N_n^2\Delta zm_n} - \frac{\psi_n-\psi n+1}{N_{n+1}^2\Delta zm_{n+1}}), & n = 2....N \\ \frac{f^2}{\Delta z_{N+1}}(\frac{\psi_N-\psi_{N+1}}{N_{n+1}^2\Delta zm_{n+1}}), & n = N+1 \end{cases} \tag{3.10}$$

where $N + 1$ is defined as the total number of discrete levels. The results is a tridagonal matrix. When solving the eigenvalue problem, the eigenfunctions represents the baroclinic modes. We define the eigenfunctions as a matrix $\vec{\psi} = F = [F1(Z_{modes}), F2(Z_{modes}), ..., FN(Z_{modes}]$, where $F1$ is the first baroclinic mode, $F2$ is the second baroclinic mode and so on.

We remember that for a flat bottom ocean a Neumann type boundary condition is used $\frac{\partial\psi}{\partial z} = 0$ for $z = 0, -H$. A staggered grid is for this case a suitable choice. For a steep bottom however the bottom boundary condition is changed to a Dirichlet type where the velocities are equal to zero at the bottom of the ocean ($\psi = 0$ for $z = -H$). The change in boundary condition makes the staggered grid unsuitable as it gives us grid points below the sea floor. Obviously we do not have values for N^2 at this "ghost depth". With the flat bottom boundary condition the term involving this depth is defined to be zero. For the steep bottom that is not the case. When calculating steep bottom modes we therefore have to alter the finite difference approximation to a non-staggered grid.

Errors introduced by numerical solutions

In the procedure of modal decomposition we had to do several interpolations, both because of lack of data and because of the need for orthogonality. From text books we know that each time we interpolate we introduce an error dependent on the interpolation method used. The first interpolation we do is to interpolate the temperature and salinity field form a one degree resolution to the latitude and longitude

of the moorings. Then the Brunt-Väisälä frequency has to be interpolated onto an uniformly spaced grid to obtain orthogonality. The grid is defined using linear spacing from the surface to the sea floor depth. The modes are calculated on the mid depths, so that if N^2 lies on Δz, the modes will be on the grid $\Delta z + 1/2$. In order to project the velocities onto the modes, we had to interpolate the velocities onto the grid used for the modes. This is problematic when we do not have velocity measurements close to the bottom. Several extrapolation methods was tested, but they all had a tendency to introduce a zero-crossing, which is undesirable as it introduces a higher order mode. We chose to let the lowest measurement available be equal to the velocity at the bottom. In oceanography it is often assumed that velocities are small and close to constant in the deep layer. However, when using this approximation we are "forcing" part of the water column to be barotropic. The reader should keep this in mind when interpreting the results. In table 4.1 the sea floor depth and the depth of the deepest observation is given.

When calculating the modes it is in reality only possible to calculate as many modes as we have records in the vertical. One can think that the water column is divided into layers where each record represents the average velocity in its respective layer. If we have records from 4 depths, or 4 layers, we can only calculate the barotropic mode and 3 baroclinic modes for the flat bottom case and four baroclinic modes for the steep bottom case. When we interpolate onto a uniformly spaced grid however, we have chosen to use a resolution of a 100 points in the vertical. That gives us 99 baroclinic modes. We will show that the first one or two baroclinic modes in addition to the barotropic mode account for almost all of the water column-averaged kinetic energy. The modes that only appears due to the interpolation is therefore not significant.

We have defined a uniformly spaced grid with layers a distance δz apart. In reality the distance between the boundary and the layer above or below for the lower and upper boundary respectively, is infinitely small. Because of this distance between the layers we are introducing a vertical error of the order δz. The horizontal error is on the order of $N\delta/f$ [Smith, 2007]. When calculating the modes on a grid that is staggered with a distance $1/2\Delta z$ from our uniform grid, we reduce the error by a factor of 2.

3.5 Modal decomposition

We want to decompose the velocity profiles into its modal components so that the relative strength of the barotropic and baroclinic modes can be found. To do so the modes should be orthonormal

$$\int_{-H}^{0} F_i(z)F_j(z)dz = \delta_{ij} \tag{3.11}$$

where δ_{ij} is the Kronecker delta and F are the baroclinic modes [Kundu *et al.*, 1975]. We know from linear algebra that "an $n \times n$ matrix, A, is orthogonally diagonalizable if and only if A is a symmetric matrix" [Lay, 2012]. A matrix is symmetric if $A^T = A$. To fulfill this requirement the grid used to calculate the modes had to be uniformly spaced. We therefore had to interpolated the Brunt-Väisälä frequencies on to an evenly spaced grid, $Z_{uniform}$.

We modes calculated also had to be normalized, which was done the following way

$$a_n = (\frac{H}{H \int_{-H}^{0} F_n^2 dz})^{1/2}, \qquad F_n = a_n F_n. \tag{3.12}$$

where H is the total depth. The modes form a complete orthogonal basis. Under the requirement of orthogonality and the assumption that $f(x)$ is a piecewise smooth function, $f(z)$ can be expanded as a series

$$f(z) = \alpha_0 + \alpha_1 F_1 + \alpha_2 F_2 + ... + \alpha_N F_N. \tag{3.13}$$

In our case $f(z)$ represents the velocity profile of the u or v component with depth when time means are removed. The coefficients α_n are defined as

$$\alpha_n = \frac{1}{H} \int_{-H}^{0} f(z) F_n dz. \tag{3.14}$$

where $n = 1, ..., N$. In order to do the integration the velocities had to be interpolated onto the same grid used for the modes. The first term on the right hand side of equation 3.13 represents the barotropic contribution. The barotropic mode is not properly resolved when solving the eigenvalue problem and has to be calculated separately. We define the barotropic contribution as

$$\alpha_0 = \frac{1}{H} \int_{-H}^{0} f(z) dz. \tag{3.15}$$

We are interested in knowing how many of the terms in the series 3.13 we need in order to reproduce the velocity profiles. To help us quantify the contribution from the different terms we find the variance.

To find the variance we make use of the Parseval identity

$$\frac{1}{H} \int_{-H}^{0} f(z)^2 dz = \sum_{n=1}^{N} \alpha_n^2. \tag{3.16}$$

This identity is the reason for why the modes should be normalized. We know from 3.11 that when taking the depth integral of the modes squared we get 1, leaving us with only the coefficients α_n^2. Each coefficient gives the contribution of the corresponding mode to the column averaged kinetic energy.

The same requirements for orthonormality has to be met also for the steep bottom case. The projection of velocities however, is not as easy as for the flat bottom case. As mentioned in the theory section the barotropic mode vanish when using steep bottom mode and instead we have a bottom trapped topographic wave. The topographic wave contributes to the vertical velocity profile, but the wave is not orthogonal to the baroclinic modes. That means that the topographic wave contribution cannot be included in the series expansion. We have

$$f(z) = T_w + \sum_{n=1}^{N} \alpha_n G_n, \tag{3.17}$$

where T_w is the bottom trapped topographic wave and G_n is the steep bottom modes. Since we only have measurements for a single point in the horizontal direction we cannot know the magnitude or the direction of the topographic wave. This makes it impossible to find the contribution from the different modes to the column-averaged kinetic energy.

By assuming that the topographic wave is large enough to be constant throughout the whole water column and equal to the lowermost measurement, we can subtract the "topographic wave contribution" from the velocity profile forcing it to go to zero at the bottom. The shifted velocity profile can then be represented by only the baroclinic modes using the same approach as for flat bottom mode. This is not very useful for this thesis as we want to compare the contribution of the barotropic and first baroclinic flat bottom mode to the contribution of the first baroclinic steep bottom mode. Since there is no way of knowing the topographic wave effect on the velocity profile we have to use a different approach.

3.6 Exponential stratification

We are interested in comparing the first baroclinic steep bottom mode to the analytic solution presented in equation 2.56. In order to solve the equation we need to know the e-folding time. This can easily be done using MatLab. We find the best exponential fit $N = N_0 e^{bz}$ from the stratification, N^2, where $b = 1/h$ is the e-folding scale. In most of the locations the stratification has a subsurface maximum (see figure 4.17). The exponential fit is done below that maximum. For this solution we are saying that the velocities vanishes with increasing depth, meaning that the solution is independent of the sea floor slope.

The dynamical modes discussed above are all dependent on the approximations done and the boundary conditions chosen. A method to look at the structure of the velocity field without making any dynamical assumptions is to use empirical

orthogonal functions, which are only dependent on the statistics of the data [Kundu *et al.*, 1975].

3.7 Empirical Orthogonal Functions

The method of empirical orthogonal functions, also known as principal component analysis is used to analyze the variability of the vertical velocity field. This gives us a picture of the dominant velocity structures. The method also gives a measure of the importance of the different patterns of variability. In this thesis the patterns are referred to as the EOFs. Since the velocity field consist of real values, the EOFs represent standing oscillations [Bjornsson & Venegas, 1997]. In our case the standing oscillations tell us something about the horizontal velocities throughout the water column.

Following Bjornsson & Venegas [1997] we organize the data into a matrix, U, where each column holds a time series of the u/v-component. The rows represent the depth of the measurements. To make the EOFs understandable we remove the time mean so that we can construct a covariance matrix, $R = U'U$. We then solve the eigenvalue problem

$$RC = C\Lambda. \tag{3.18}$$

The diagonal matrix Λ contains the eigenvalues λ_j of the covariance matrix. C holds the eigenvectors, or the EOFs, corresponding to the eigenvalues. The biggest eigenvalue corresponds to EOF1, the second biggest to EOF2 and so on. By dividing the corresponding eigenvalue by the sum of all eigenvalues we find variability that lies in each of the EOFs.

In this thesis we are looking at the EOFs as the "true" structure and the different dynamical modes are superimposed on to the EOFs to see if they capture the structure at the particular locations.

Chapter 4

Results and Discussion

In this section we are looking at the results and highlights the similarities and differences we find in comparison with W97. We start by looking at the fitting procedure before we discuss the flat bottom case. The empirical orthogonal functions are introduced and we compare the most dominant EOF with the baroclinic modes found from different approaches. The results are presented by moorings, and the location and mooring numbers are marked on figure 3.1. Basic information about each mooring is given in table 4.1 and more detailed information is given in the appendix.

4.1 The mode fits

The approach for mode fitting used in this thesis is different from W97. To verify that our method is adequate, we look at the fit for mooring 42.

We want to represent the vertical structure of the ocean in terms of dynamical modes. As we know from the theory these modes are dependent on the stratification. Figure 4.1 shows the first through fifth baroclinic modes under the assumptions of a flat bottom ocean (left) and a steep bottom ocean (right). We see that the structure in the upper 1000 m is the same for the two sets of modes. Towards the bottom the different boundary conditions start to influence the structure, and as a result the steep bottom modes have one zero-crossing less than the corresponding flat bottom modes. The modes have the largest amplitude at the surface.

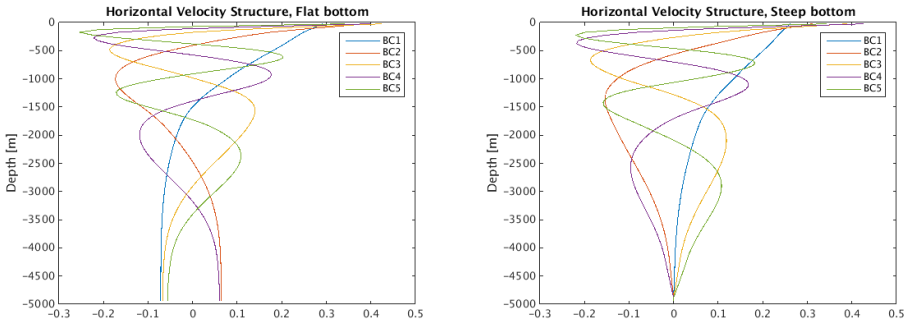

Figure 4.1: The first through fifth baroclinic modes under the assumption of a flat bottom ocean (left) and steep bottom ocean (right).

The velocities with the time mean removed are projected onto the modes. Figure 4.2a shows that we are in a quiet area of the ocean where there is little to no motion below the pycnocline. The flow in the pycnocline layer is towards north-west, with a maximum magnitude of 2.4 cm/s at 90 m depth. The velocity profiles shown are snapshots of a representative day (measuring day no 100, May 2^{nd} 1989).

The modal fitting is shown in figure 4.2b. The velocity perturbations of the u component is shown as a black line. The red line shows the perturbations with the barotropic mode subtracted for the flat bottom case and with the bottom velocity, assumed to be the topographic wave contribution, subtracted for the steep bottom case. When using 50 baroclinic modes we see from the blue dotted line that we get a perfect fit. Consequently we assume that 50 layers is equivalent to a continuously stratified ocean with infinitesimally thin layers. In reality we only have measurements from a finite number of depths much less than 50. When doing the perfect fit we are using modes that are only available due to interpolation. In the case shown in figure 4.2b we have measurements from 5 depths, represented by black circles. In reality we only have 5 modes available to represent the velocity profile. The pink dotted line shows that 5 modes gives a fairly good representation. However, in both cases the fit slightly overshots the profile. The overshooting happens between the measuring depths, and is common for moorings which have a poor instrument distribution throughout the water column. Because of this feature we are using all 50 modes when doing our analysis to ensure a perfect fit.

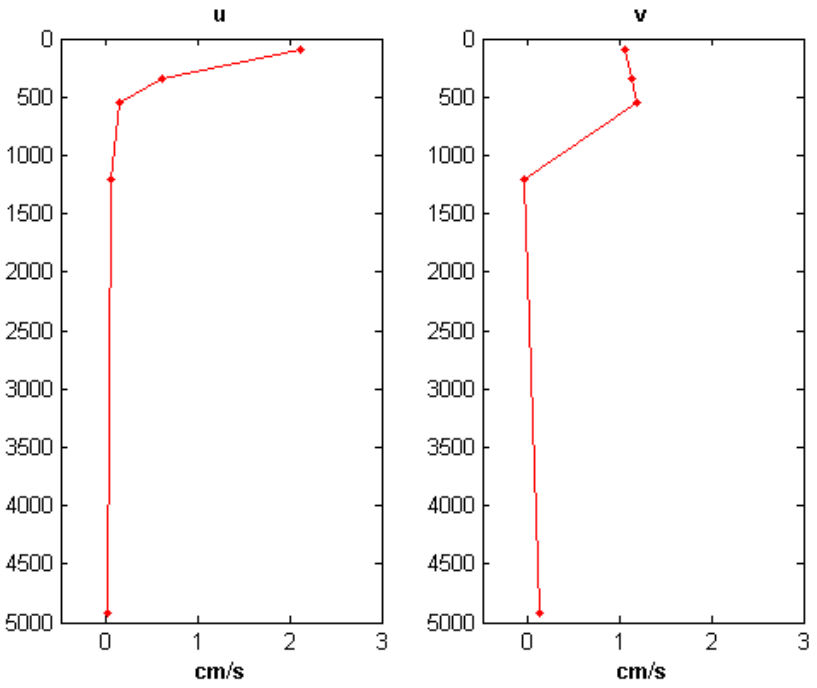

(a) The velocity components u and v on the 2^{nd} of May 1989 at mooring 42

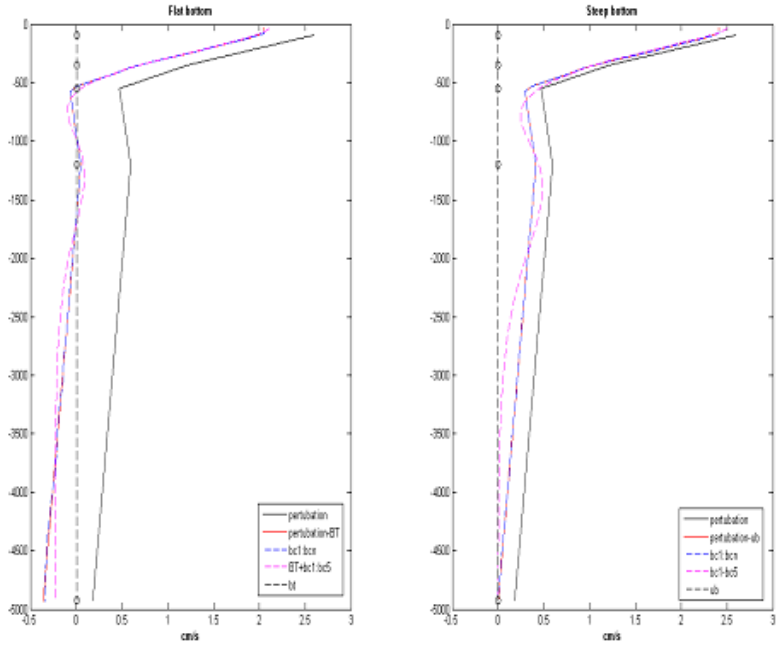

(b) The modal fit for the flat bottom case (left) and the steep bottom case (right). The black line shows the perturbed velocity profile for the u component a). The red line is the perturbed velocity with the barotropic mode subtracted for the flat bottom case and the bottom velocity subtracted for the steep bottom case. The blue dotted line shows the fit using 50 modes and the pink dotted line shows the fit using 5 modes. The measuring depths are denoted with black circles. The black dotted line is the barotropic mode and the assumed topographic wave contribution respectively.

Figure 4.2: The mode fit for mooring 42

4.2 Flat bottom modes

Table 4.1 shows the percent of kinetic energy in the barotropic mode and first baroclinic mode for both the u and v components, calculated assuming a flat bottom ocean. On average 46% of the column averaged kinetic energy is in the barotropic mode and 29% of the kinetic energy is in first baroclinic mode.

In order to make a flat bottom assumption the mooring should be in waters of at least 4000 m depth [Wunsch, 1997]. For this thesis we are interested in knowing how topography is affecting the results, and have therefore included calculations for shallower locations. Figure 4.3 shows the fraction of kinetic energy in the barotropic mode (blue) and in the first baroclinic mode (green) versus the sea floor depth. The energy partition does not seem to be influenced by the depth of the waters. In other words, the assumption of a flat bottom seems to give reasonable results also when the depth is shallower than 4000 m. To convince us even further that the bottom depth is insignificant in the comparison with W97, we calculated the average fraction of energy for all moorings that are located in waters of 3500 m or deeper (consistent with the data analyzed by Wunsch). The average was the same for the barotropic mode, and reduced by only 1% for the baroclinic mode.

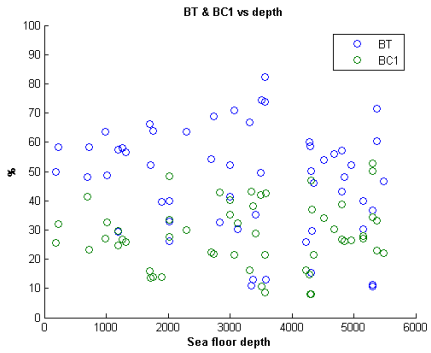

Figure 4.3: A scatter plot of the percent of the kinetic energy in the barotropic mode (blue) and in the first baroclinic mode (green) with sea floor depth.

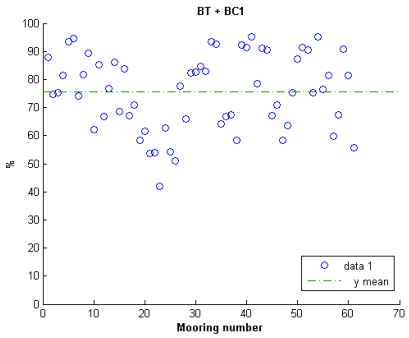

(a) The percentage in the barotropic and first baroclinic modes together for the 61 moorings. The dashed line shows an average of 72%.

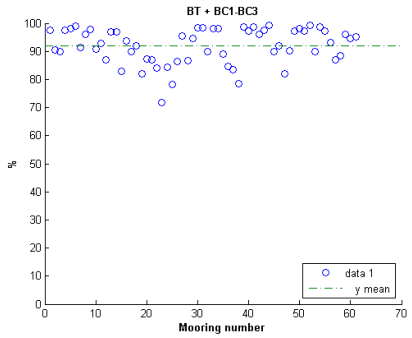

(b) The percentage in the barotropic and the first three baroclinic modes together for the 61 moorings. The dashed line now shows an average of 91%.

The fraction of kinetic energy of the u component in the barotropic and first baroclinic mode together is shown in figure 4.4a. The dashed line shows an average of 72%. The lowest value is 42 % and the highest is 95%. The results are plotted against the mooring number. To get an average of over 90% we need to include the second and third baroclinic modes. On average these modes accounts for 11% and 5% of the kinetic energy respectively. We see from figure 4.4b that for some of our mooring locations, higher order modes account for more than 20% of the energy. A common factor for these locations is that they have several measurements in the upper 300 meters.

Wunsch is presenting his results by areas. In most of the areas he finds that the barotropic and first baroclinic modes accounts for as much as 90% of the energy. On a general basis the first baroclinic mode contributes the most. This is a contradiction to what we are finding. Only one of the moorings in this study have the same latitude, longitude and number of days as any of the moorings used in W97. Wunsch finds the flow in this location to be 59 (47) % barotropic for the $u(v)$ component, whereas we find it to be 52 (52) %. For the first baroclinic mode Wunsch finds it to account for 22 (31)% of the energy, and our result is 26 (31)%. From this one case it looks like our method gives a slightly higher percentage in the baroclinic mode than Wunsch's method. This is not in agreement with the average results which shows that we are underestimating the energy contribution from the first baroclinic mode compared to W97.

Wunsch has an advantage in the number of mooring locations available for analysis. With several moorings from the same region you can make a representative average for the different parts of the ocean. The characteristics of the areas with a good coverage will have a bigger weight when looking at the ocean as one. One should therefore be careful with drawing global conclusions when the results are not evenly representative for all areas. The data available for this thesis is quite spread out, and most of the moorings have been located not far of from the coast. We also have several moorings north of 60°N. Some of the northern regions are found to be barotropic in character, and contributes to raising the average of the barotropic mode.

4.2.1 Regional Dependence

We know from the Sturm-Liouville equation that the vertical structure depends on N/f, where N is the Brunt-Väisälä frequency and f is the Coriolis parameter [Talley *et al.*, 2011]. At high latitudes the stratification is weak and the Coriolis parameter is large. We would therefore expect the barotropic mode to become more important at higher latitudes. Figure 4.5 shows the percentage of energy in the barotropic mode and in the first baroclinic mode with latitude. We see that the barotropic mode on average dominates over the barotropic mode. However, we do not see an obvious trend of the modes getting more barotropic with latitude. The

results from the Arctic ocean (latitudes close to 90°) is proving to be less barotropic than the Greenland Sea and Labrador Sea. The results in this thesis point towards an area dependence more than a latitude dependence.

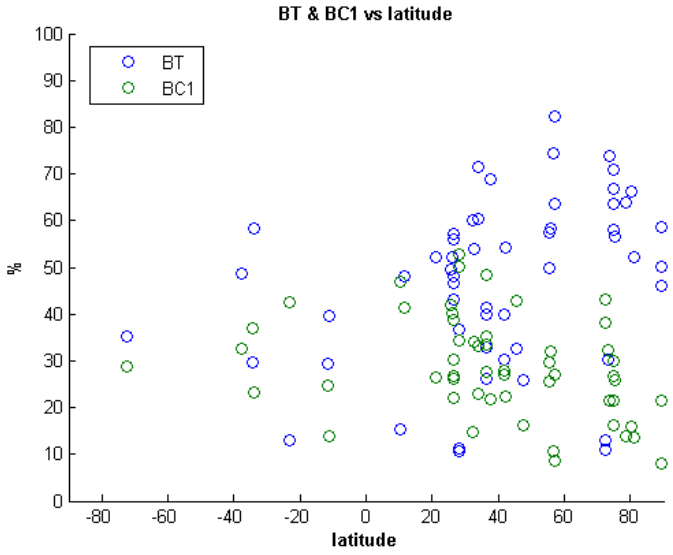

Figure 4.5: Percent of kinetic energy in the barotropic mode (blue) and first baroclinic mode with latitude

The Arctic Ocean

We have measurements from three different areas in the Arctic Ocean. The northern most area have an average of 50% in the barotropic mode and 13% in the first baroclinic mode. The moorings north of the New Siberian Islands shows a slightly more barotropic area with an average of almost 60% against 15% in the first baroclinic mode. In the Baufort Sea, on the other hand, the first baroclinic mode dominates with an average of around 35% and with only 15% of the kinetic energy in the barotropic mode.

The Greenland Sea and The Labrador Sea

Measurements form the Greenland Sea and the Labrador Sea both shows a barotropic dominance. For the Greenland Sea the average is close to 60% and in the Labrador Sea the average is almost 80%. The only mooring that does not show a highly barotropic dominance is number 24. This is the easternmost mooring in the Greenland sea and for this particular mooring the baroclinic flow contributes just as much as the barotropic.

The North Atlantic

We have several measurements from the east coast of North-America. In the Gulf of Mexico we have a barotropic and a baroclinic flow of equal importance, both being close to 50%. Outside of the gulf the barotropic contribution stays the same, but the first baroclinic decreases to 30%. Further north and close to the coast we have a decrease in the barotropic mode to 40%. A little outside of the coast the barotropic mode accounts for almost 60%. Figure 4.6 shows Wunsch's results from the North Atlantic for the barotropic mode. We see that the results we find are very much like what is pictured in the figure.

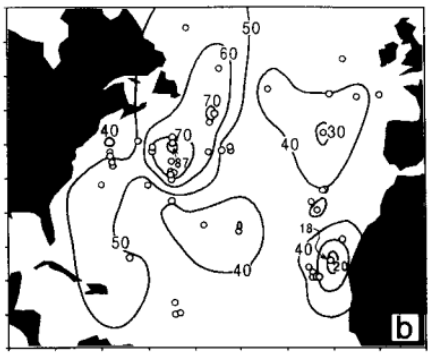

Figure 4.6: Percent of kinetic energy in the barotropic mode in the North Atlantic found by Wunsch [1997].

The North Pacific

In the North Pacific the first baroclinic mode is ranging from 30 - 40%. We find that most of the west part of the North Pacific is 30% barotropic. This is in agreement with Wunsch. The Gulf of Alaska is 55% barotropic and we find that the measurements outside of California is 50% barotropic. Unfortunately we only have measurements east of 200°W.

By looking closely at the results from W97 we see that several of the moorings analyzed for this study actually lies in areas where the barotropic mode gives the highest contribution to the energy. This might be the reason for why we do not see a clear latitude dependence and for why our average statistics are not in agreement with W97. Guinehut *et al.* [2006] is using altimeter sea level anomalies from satellite data, and hydrographic height anomalies calculated from *in situ* temperature and salinity to look at the vertical structure of the ocean. They find an energy partition highly dependent on latitude. Cabanes *et al.* [2008] support this analyzing data from argo floats. They also find that the barotropic mode is dominant south of 40°S, from where we only have one mooring.

4.2.2 Time variations

The modal analysis has shown that the partition of energy between the different modes is highly variable in time. Figure 4.7 shows time series of the barotropic and first baroclinic contribution for the east-west component, at mooring 14. We see that the two modes tend to compensate each other. When the barotropic mode

drops, the baroclinic mode spikes. The correlation coefficient between the two modes is $r = -0.85$. The result is varying from being close to 100% barotropic one day to almost a 100% barotropic a few days later. This variability is found at almost all our locations. For the case shown the average kinetic energy in the barotropic mode and first baroclinic mode is 56% and 30% respectively, with corresponding standard deviations as high as 33% and 30%.

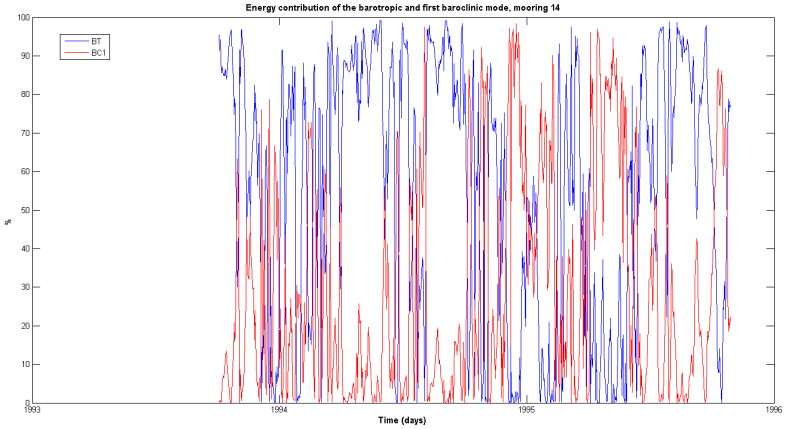

Figure 4.7: The partition of kinetic energy in the barotropic mode (blue) and baroclinic mode (red) with time for mooring 14

For clarity we have only plotted the barotropic and first baroclinic mode. The higher order modes have on a general basis decreasing averages, and monotonically decreasing maximum peaks. For the chosen location the average kinetic energy is 6.6% in the second baroclinic mode, with a maximum peak of 82.5%. For the third baroclinic mode the average is 4.2% and the maximum peak is 58.0%. This shows that also the higher order modes are highly variable in time. The second baroclinic mode the barotropic mode are slightly anti-correlated with a correlation coefficient of -0.53. The first and second baroclinic mode together have a correlation of -0.92 with the barotropic mode. The higher order modes are not correlated in any way (r $\approx$ 0).

Scott & Furnival [2012] point out the shortage of variability analysis W97. They are using data from simulations and when doing modal analysis they find the same features as we do from the observational data, namely a barotropic mode varying from close to 100% one day to almost zero a few days later. For this thesis we are following Wunsch and only present mean statistics. It should however be noted that the large variability about the mean is of great relevance when interpreting altimeter data.

4.2.3 Difficulties

As mentioned in section 4.5 the lack of seasonal variations for the dynamical modes can influence the result. We have used several locations where seasonal variations are prominent, i.e. the Labrador Sea, the Arctic and the Greenland sea. These locations are under the influence of freezing in the winter and considerable freshwater input from land in summer. To make a conclusion about the vertical partition of energy in areas with strong seasonality, one should analyze longer time series by season [Wunsch, 1997]. Unfortunately our time series do not have the duration to be analyzed by season, and the same approach has been used for all moorings.

The distribution of kinetic energy between the modes does not only change with season, but also with years. Müller & Siedler [1992] analyzed among others, a mooring (KIEL276, 33N, 22W) that has records for almost nine years. They find changes in primarily the zonal component with a 3-4 years period in addition to a directional dependent energy distribution with a period of about 200 days. That shows that we need long time series in order for the results to be statistically significant. Unfortunately most of the records we have available does not even cover one year.

In addition to variabilities in time it is also a challenge that the data available is so variable in quality and in distribution throughout the water column. During the process of analyzing the data sets we have come upon several velocity profiles that behave unexpectedly. When using an archive like the GMACMD, with data from different projects and from different decades it is hard to know if unexpected values are noise, or if the results are legit. We have chosen to use data that on average produces reasonable results and anomalous days are excluded.

As mentioned above locations with several instruments near the surface have a tendency to have a larger percentage of kinetic energy in the higher order modes. We know that every time the velocity profile crosses zero we introduce a new order of modes. The surface layer has a complicated structure due to direct atmospheric forcing. This often results in several zero-crossings, and hence more energy in higher order modes. This typical behavior of the surface layer is not captured when we have a poor vertical distribution of instruments.

Table 4.1: Basic information about the moorings analyzed; latitude, longitude, percentage of mean kinetic energy in the baroclinic and first barotropic modes of the u and v component, sea floor depth and the deepest measuring depth.

Mooring no	Latitude	Longitude	BT_u	BC1_u	BT_v	BC1_v	Sfdepth	Deepest inst
1	32,7010	231,9380	53,8	33,9	57,3	29,4	4524	1481
2	32,1550	231,9920	60,2	14,6	52,1	23,5	4280	1419
3	45,4560	228,8230	32,5	42,7	34,6	38,4	2836	2500
4	-37,6700	167,2700	48,6	32,7	46,7	31,8	1014	1004
5	34,0370	289,9570	60,2	33,1	54,2	32,3	5366	4000
6	33,9770	289,9930	71,6	22,9	44,7	44,4	5366	4000
7	26,4890	283,5520	48,0	26,1	61,5	21,6	4850	3800
8	26,4750	283,8980	43,0	38,6	38,7	44,1	4810	3800
9	11,3800	53,0100	48,1	41,3	33,3	46,6	700	645
10	10,2000	53,6300	15,4	46,9	28,6	32,3	4305	4230
11	56,7530	307,5450	74,4	10,8	82,7	8,0	3510	3476
12	-34,5430	333,0250	29,8	36,9	25,0	37,6	4325	4310
13	42,2670	349,8500	54,3	22,5	55,6	25,2	2700	2000
14	26,4980	284,3170	55,9	30,2	44,2	41,2	4689	4000
15	26,4870	288,8330	43,7	12,1	49,3	13,0	5488	4000
16	26,5000	283,9000	57,1	26,8	54,5	25,5	4807	4000
17	41,9720	207,9930	40,0	27,2	38,9	24,6	5150	3756
18	27,9980	208,0520	36,8	34,3	37,7	40,0	5300	3919
19	41,9900	207,9450	30,2	28,1	24,3	28,0	5150	3980
20	28,0330	207,9000	11,3	50,2	30,2	47,6	5300	3984
21	-11,2670	122,9170	39,6	14,0	28,4	21,3	1895	1400
22	-11,4170	122,9830	29,5	24,6	26,2	24,8	1197	870
23	47,4230	220,7030	25,7	16,3	29,1	16,0	4224	3999
24	73,3860	359,1720	30,4	32,3	24,1	28,9	3131	2472
25	72,6200	216,4320	11,0	43,2	23,9	29,8	3339	1534
26	72,5420	216,1700	13,1	38,0	15,0	34,6	3370	1500
27	78,5130	133,9620	64,0	13,8	62,8	14,1	1761	1161
28	81,0750	138,9000	52,1	13,7	52,5	17,5	1712	1692
29	80,3200	150,0570	66,3	16,0	47,2	22,1	1699	1109
30	75,4980	348,8780	56,6	26,0	45,4	33,5	1312	1307
31	75,0780	347,8470	58,1	26,6	47,4	35,2	1263	1242
32	74,9930	350,8980	66,9	16,1	64,7	12,3	3317	3253
33	74,9710	348,4160	63,5	30,0	60,7	31,0	2300	2188
34	74,9930	349,3920	71,0	21,4	74,1	19,0	3075	2971
35	-72,5570	339,4050	35,3	28,8	40,8	41,8	3415	3411
36	89,4550	54,3290	58,7	7,9	56,3	9,3	4295	2508
37	89,2530	64,6920	46,1	21,4	49,0	19,4	4345	4336
38	89,3470	77,1200	50,3	8,0	43,5	10,3	4315	4306
39	25,8720	265,1200	52,2	40,1	37,7	55,4	3000	1500
40	25,4920	265,8400	49,5	41,9	52,6	39,0	3500	3000
41	73,8290	355,1660	73,7	21,6	63,2	28,6	3570	1503
42	21,2166	335,5767	52,1	26,5	52,3	31,3	4960	4920
43	56,9567	308,4117	82,3	8,8	73,4	13,2	3560	3545
44	57,1150	350,6367	63,5	27,0	63,6	25,8	992	892
45	41,9717	207,9933	39,9	27,2	38,9	24,6	5150	3756
46	27,9983	208,0517	36,8	34,2	37,7	40,0	5300	3919
47	41,9900	207,9450	30,3	28,1	24,3	28,0	5150	3980
48	28,0333	207,9000	10,8	52,9	36,0	44,2	5300	3984
49	55,4057	203,6668	49,9	25,5	63,0	17,9	190	172
50	55,3688	204,9375	57,5	29,7	48,7	28,8	1189	1000
51	25,4917	265,8400	49,4	41,9	52,6	39,1	3500	3000
52	55,9571	203,6227	58,3	32,2	53,5	35,0	227	202
53	45,4563	228,8227	32,5	42,8	34,6	38,6	2836	2506
54	73,8287	355,1663	73,7	21,6	63,2	28,6	3570	1503
55	36,3050	286,2718	41,3	35,1	33,9	42,6	3006	1200
56	36,2517	285,6733	32,9	48,4	45,1	38,2	2020	1900
57	36,2517	285,6733	26,2	33,6	55,6	22,6	2020	1900
58	36,2517	285,6733	39,8	27,5	49,1	28,2	2020	1900
59	37,5842	4,4983	68,8	21,9	55,3	31,4	2738	2000
60	-33,9850	114,4150	58,2	23,1	69,4	20,5	720	320
61	-23,3067	48,5700	12,9	42,7	47,3	26,8	3580	2983

4.3 Empirical Orthogonal Functions

When projecting velocities onto dynamical modes we are making assumptions about what the structure ought to look like. By using empirical orthogonal functions we are able to look for patterns in the velocity data without making any assumptions about the structure. Figure 4.8 shows EOFs for three different areas, and their corresponding current time series for the u component in selected depths. The moorings are chosen for their different characteristics, and the locations are shown in figure 3.1.

The first case is from a mooring that was located near Africa from January to October 1989 (mooring 42). The EOFs (figure 4.8b) shows a pattern very much like what we expect from steep bottom modes (see figure 4.1). EOF1, which accounts for as much as 89% of the variability resembles the first baroclinic mode. The second EOF looks like the second baroclinic mode and the third EOF like the third baroclinic mode. We see from both the velocity time series and the plot of the EOFs that the velocities are approaching zero towards the bottom. In this location a pattern that resembles a topographic wave (largest velocity at the bottom with en exponential decrease with decreasing depth), shows up in EOF5 and only accounts for 0.4% of the variability (not shown). The velocity time series shows a good correlation between all layers except the one at 4920 m (4.8a). The sea floor depth is 4960 m, so the decrease in correlation could be due to friction at the bottom. It could also be an indication of the presence of a weak topographic wave. It is also worth noticing that the velocity in the lower levels are quite small. The instrument type used for this location is not available, but considering the year (1989) and number of instruments used (5) it is reasonable to assume that a mechanical sensor was used. These instruments have, as discussed in chapter 3.2 a threshold and velocities smaller than 1-2 cm might be poorly represented.

The second case is from a mooring in the South Atlantic (mooring 12). From the EOFs we see that the most dominant EOF also in this case looks like the first baroclinic steep bottom mode. The EOF2 resembles a topographic wave that is dominating the flow in the lower 1000 m of the water column. We know from equation 2.45 that topographic wave will not cross the zero line as EOF2 does. The crossing could be due to noise, or it could be a coupling with a different mode. From the velocity time series we clearly see that the bottom velocities increases towards the bottom. It is also a bad correlation between the two deepest measurements. This point to the existence of a topographic wave. The sea floor depth at the location is 4325 m and the measurements were done from December 1992 to April 1994. An ADCP was used for the upper measurements, and a vector averaging recording current meter (RCM 8) was used for the deeper ones.

The third case is from the Labrador sea (mooring 43). The EOFs shows a profile

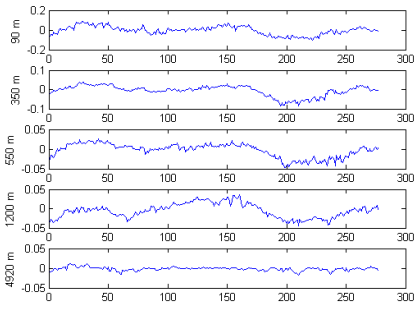

(a) Velocity time series of the u component in m/s at the location of mooring 42.

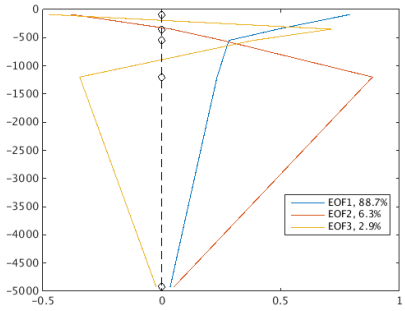

(b) The first, second and third EOF and the explained variance for mooring 42.

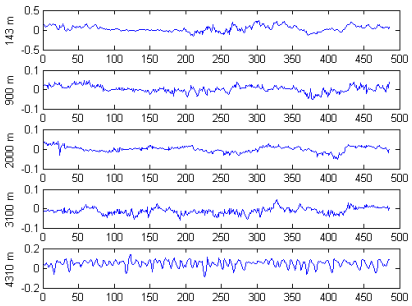

(c) Velocity time series of the u component in m/s at the location of mooring 12.

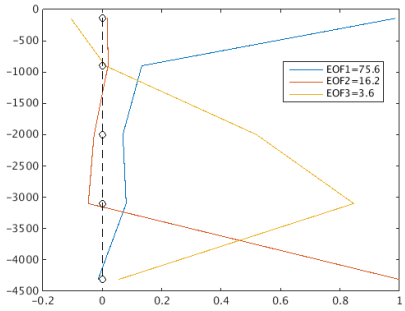

(d) The first, second and third EOF and the explained variance for mooring 12

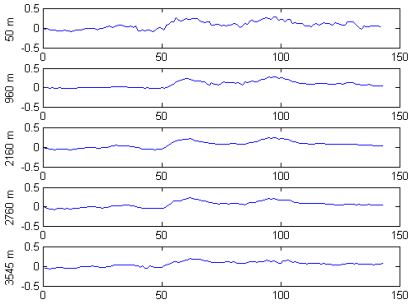

(e) Velocity time series of the u component in m/s at the location of mooring 43.

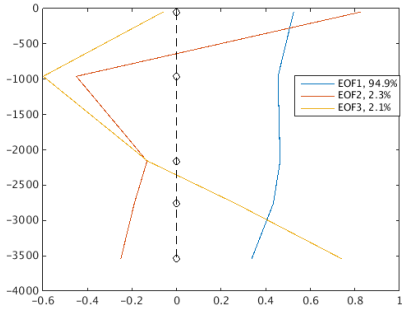

(f) The first, second and third EOF and the explained variance for mooring 43

Figure 4.8: Time series from selected depths presented to look at the correlation and the corresponding EOFs where the 3 most dominant structures are shown.

different from the two cases above. EOF1 accounts for as much as 95% and seems to be some kind of barotropic response. The EOF2 bear resemblance to the first baroclinic flat bottom mode. Figure 4.8e shows a flow that is not changing much throughout the water column. The correlation coefficient between the measure-

ments at 50m depth and 3545 m is 0.8749. This barotropicity is consistent with what we found form the flat bottom mode analysis. The measurements are from June - December 1987 and the mooring lies in waters of 3560m depth.

EOFs have been computed for all of the moorings analyzed. We find that the structure of EOF2 and higher varies a lot between locations. EOF1 however, with the exception of the Labrador Sea and some moorings in the Greenland sea, show more or less the same shape for all locations. It resembles the first baroclinic steep bottom mode, and on average accounts for 75% (see figure 4.9). The highest variance found in EOF1 is from the Labrador Sea where it accounts for more than 90%. The lowest contributions are from shallow areas where the flow is more complex in character.

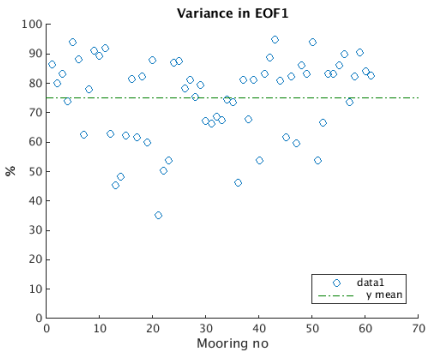

Figure 4.9: The variance explained by EOF1. The dashed line shows an average of 75%.

Various forms of Empirical Orthogonal Functions have been used in several studies regarding modal decomposition (e.g Kundu *et al.* [1975], De Mey & Robinson [1987], Müller & Siedler [1992] and many others). The method is a great tool for analyzing mooring data when looking at vertical structures. However, it is not obvious how to extend this information to locations where moorings have not been deployed. W97 is also doing EOF analysis and finds the most dominant structure to be a combination between the barotropic and first baroclinic mode. Figure 1.1 shows, as mentioned in the motivation, a typical EOF1 found both in this study, by W97 and also in literature. It is argued that the results for EOFs are misleading as they point towards a strong coupling between the barotropic and first baroclinic mode, which is not necessarily what is happening. We are proposing that EOF1 might be the first baroclinic steep bottom mode instead of the two coupled modes.

Another reason for why W97 did not find EOFs useful is that there is no straightforward way to extrapolate the EOFs to the surface. De Mey & Robinson [1987] looked into using EOFs to extrapolate the surface signal below the surface and in order to do so one have to rely on historical knowledge of the local current statistics. For this study however, we are only interested in the structure of the EOFs. When we know the dominant structure we can investigate if there is any way to predict the shape of the vertical variability.

4.4 First baroclinic mode structures

In section 4.2 we looked at the partition of horizontal kinetic energy between the barotropic and first baroclinic mode assuming a flat bottom with realistic stratification. We are interested to see what effect the topography has on the vertical modes, and for this thesis we are considering rough topography. That is, a steep bottom slope with depth changes comparable to the length scale of the motion [Samelson, 1992]. The effect of topography on the flow is among others studied by Dickson [1983], who analyzed eddy kinetic energy observations from 35 moorings and found weak abyssal flows for steep bottom slopes, which is consistent with the steep bottom modes having no flow at the bottom of the ocean. Samelson [1992] suggested that rough topography is a necessary (but not sufficient) condition for the surface-intensification of kinetic energy found in both observations and numerical studies. We find that the shape of the most dominant EOF often resembles the first baroclinic steep bottom mode. If the flow of the ocean is dominated by the first baroclinic steep bottom mode (and a topographic wave) rather than a coupling between the barotropic and first baroclinic flat bottom mode, that is a considerable improvement conceptually when it comes to interpreting the altimeter data.

In this section we want to investigate if there is a way to successfully predict the vertical structure of the variability in a velocity field. We do this by comparing the different first baroclinic modes to the most dominant EOF. The focus will be on the steep bottom mode and the analytical solution with exponential stratification where the velocities are assumed to vanish with increasing depth. The figures in this section (4.10-4.14) shows the steep bottom mode and the analytical solution with exponential stratification superimposed onto EOF1. The blue line represents the EOF1, the pink line the first baroclinic steep bottom mode and the green line the analytical solution. The black circles denotes the instrument depths available for the different moorings. We start by looking at the same locations as we studied in section 4.3.

Figure 4.10 shows that we are able to partially capture the structure at mooring 12 when using the analytical solution. This mooring has a particularly deep stratification and the Brunt-Väisälä frequency is a factor 10 larger at the bottom than it is for any other location used. Mooring no 43 and 42 do not have a good fit. Nonetheless, the figures show some general results that are worth pointing out.

We see that the analytical solution has a shallower stratification than the steep bottom mode. In fact there is a tendency for the steep bottom mode to be deeper than the stratification shown by the EOFs. In the pycnocline layer the analytic solution has a slow decrease towards zero, whereas the steep bottom mode has a steeper decrease. We rarely get a good fit below the pycnocline layer. A common picture is that the analytic solution decreases too rapidly (or disappears), and the steep bottom mode has a too slow decreasing rate. We find that the assumption of vanishing

motion with increasing depth results in modes that go to zero around the depth of the bottom of the pycnocline layer, usually between 1000 - 2000m depth. The steep bottom modes are defined to be zero at the bottom of the ocean resulting in the slower decrease in the deep layers.

We also find that for the barotropic areas, like mooring no. 43, we do not find a good fit for any of the methods used in this thesis.

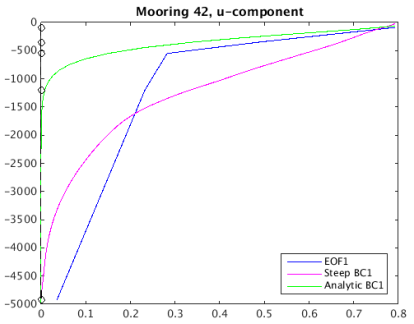

(a) Mooring 42, u component.

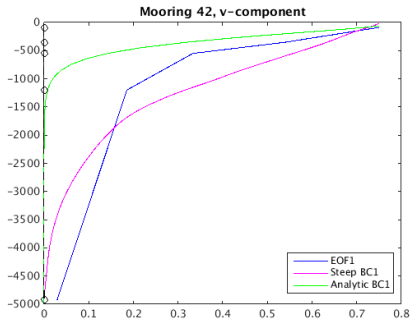

(b) Mooring 42, v component.

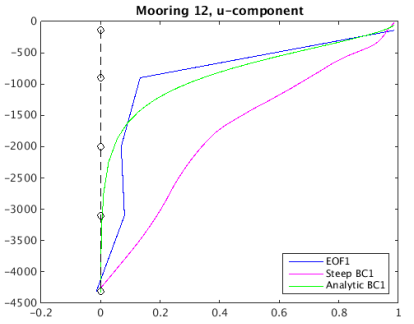

(c) Mooring 12, u component.

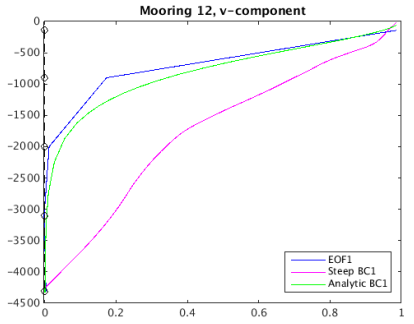

(d) Mooring 12, v component..

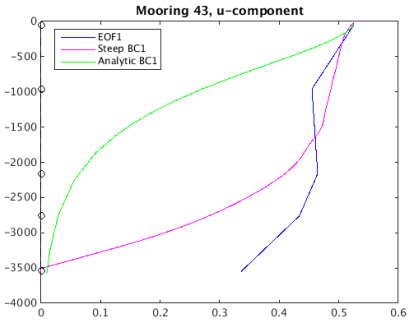

(e) Mooring 43, u component.

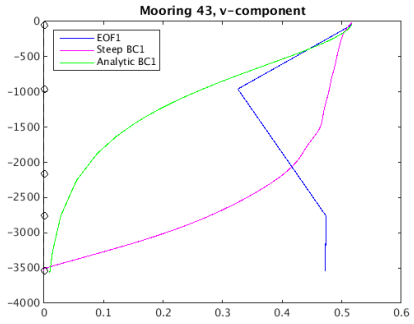

(f) Mooring 43, v component.

Figure 4.10: The dominant EOF (blue), the first baroclinic steep bottom mode (pink) and the first baroclinic analytical solution (green) from mooring 42, 12 and 43. The u component is shown on the left hand side and the v component on the left. The black circles denotes the measuring depths.

4.4.1 Regional dependence

Also when comparing the different first baroclinic mode structures to EOF1 we find that different areas gives different results. In the North Atlantic and the Pacific we were able to find approximate fits. North of 60°N, in shallow areas and close to the shore however, we are not able to capture the dominant structures.

The Atlantic ocean

The measurements from the Atlantic Ocean shows varying results. In the Gulf of Mexico and along the east coast of North America (mooring 5-8, 14-16, 39-40 and 51) we find that steep bottom modes gives a better fit than the analytical solution which is too shallow. The zonal structure from mooring 5, 8 and 51 are shown in figure 4.11. We have also included mooring 42 which is located on the east side of the Atlantic for comparison.

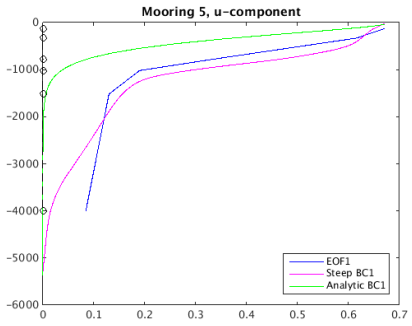

(a) The east coast of North America (mooring 5, u component).

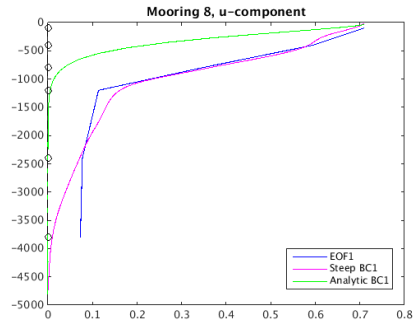

(b) The east coast of North America (mooring 8, u component).

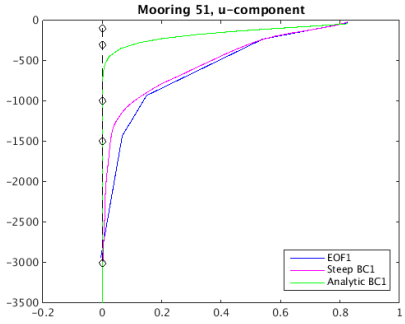

(c) The Gulf of Mexico (mooring 51, u component).

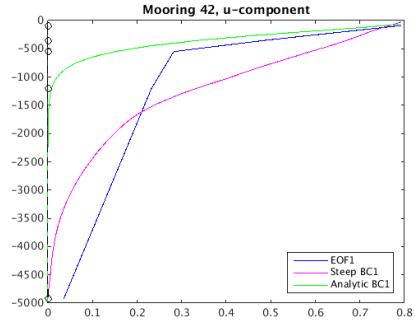

(d) The coast of Africa (mooring 42, u component).

Figure 4.11: The dominant structure in the North Atlantic and the first baroclinic modal fits.

For mooring 5 we see that the steep bottom mode is close to capture the structure throughout the pycnocline layer. The stratification is however a few meter too deep. The mode has an intensification towards the surface that we do not see from the EOF1. The mooring was deployed from May 1982 - April 1983 and the sea floor depth is 5366 m. We only have measurements down to 4000 m, which is why the EOF is ending at a shallower depth than the baroclinic modes. Mooring 8 shows a very good fit between the EOF1 and the steep bottom mode in the upper 1200 meters. The measurements was recorded from October 1988 - July 1989 and the sea floor depth is 4800 m. Also for this location we do not have measurements from the deepest 1000 m available. In the Gulf of Mexico we get a close to perfect fit between the the steep bottom mode and EOF1. The records are from June - October 1985.

The remaining moorings from the adjacent areas (but different time periods) shows the same deviation between the EOF1 and the analytical solution, making the steep bottom mode the best fit. Mooring no. 55-58 lies in shallow waters, which will be discusses in section 4.4.2. Unfortunately we only have one good mooring from the east side of the North Atlantic Ocean (mooring 13 and 44 are showing complex structures and the flow is likely to be influenced by the location very close to the coast). Figure 4.11d shows that the analytical solution gives a better approximation to the structure in the upper ocean. This picture is more similar to what we find for the Pacific Ocean.

The Pacific Ocean

The moorings in the Pacific Ocean in general point towards a shallower stratification than the results from the North Atlantic. Figure 4.12 shows the meridional structure from mooring 45, 48 and 2, and the zonal structure for mooring 3. The analytical solution is able to capture the structure in the upper $\sim$20% of the water column quite well. The decrease towards zero however, is too steep so the structure in the deep layer is badly represented. The steep bottom mode gives a stratification that is too deep for all four locations. None of the moorings in the Pacific have measurements near the bottom. Mooring 2 only have records down to 1500m even though the ocean is deeper than 4000 meter in the area.

The structure of all the moorings in the Pacific show similar features excluding those in the Gulf of Alaska which are located in very shallow waters. The results from this are are too complex to be represented by a single mode. Also the moorings located outside of the regions discussed shows a tendency for the analytical solution to give a better representation of the structure in the pycnocline layer than the steep bottom mode.

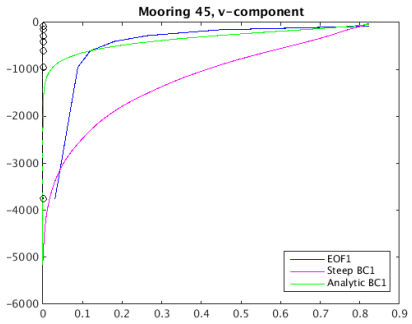

(a) Mooring 45, v component

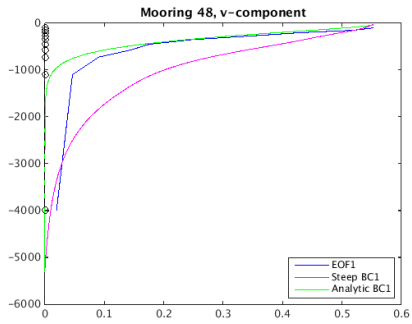

(b) Mooring 48, v component

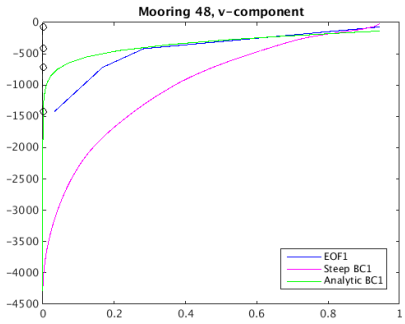

(c) Mooring 2, v component

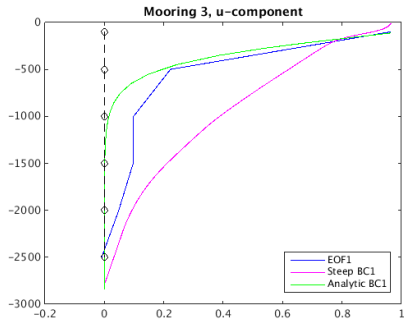

(d) Mooring 3, u component

Figure 4.12: The dominant structure in the North Pacific and the first baroclinic modal fits.

The Labrador sea

We find the Labrador Sea to be barotropic and we remember from the figures 4.10e-4.10f that the structure from mooring 43 resembles what we would expect from traditional flat bottom modes, with a barotropic mode and a first baroclinic mode with one zero crossing. We therefore include the second EOF (red) and the superimpose the first baroclinic flat bottom mode (light blue) onto the plot. The result is shown in figure 4.13. As we can see the first baroclinic flat bottom mode and EOF2 do not match, nor do the steep bottom mode or the analytical solution and EOF1. A similar picture is obtained from mooring 11 (not shown). It seems like we are not able to predict the dominant structures when we are in areas of barotropic character.

From the EOF1 it looks like the velocities are slowing down at the bottom. The lowest records are in this location only 15 meter from the bottom. When flows are dominantly barotropic the moorings are more prone to vertical displacements [Wunsch, 1997]. One explanation for the relatively strong velocities at the lowermost measuring depth could be that the assigned depth does not correspond to

the actual measuring depth due to vertical displacement. Unfortunately pressure records are not available to confirm or refute so this remains a speculation.

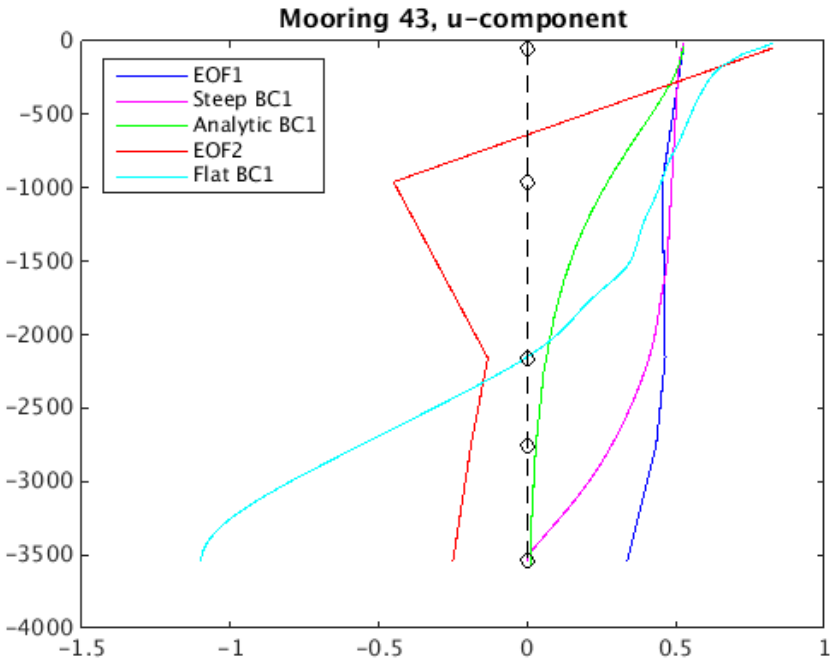

Figure 4.13: The dominant zonal structures from mooring 43. The red line represents the second most dominant EOF and the light blue line is the first baroclinic flat bottom mode.

The Arctic Ocean

The Arctic Ocean shows a complex structure throughout the water column for all moorings. The results from mooring 26 and 38 are shown in figure 4.14. The tendency in the structures resembles a first baroclinic shaped structure. Contrary to what we have seen previously the steep bottom mode shows a stratification just as shallow as the flat bottom mode. Both modes have a good fit in the pycnocline layer at mooring 26. At mooring 40 shows the steep bottom modes is starting the decrease towards zero too soon and only capture the structure in the upper few meters.

Bottom currents seems to be important for the northern most locations. By ignoring most of the measurements in the upper 200 meters for mooring 36-38 (not shown), we find that bottom velocities are significant. When the surface intensification is ignored the structure seems to be dominated by the structures of a topographic wave

and a higher order mode. Unfortunately we do not have measurements towards the bottom for any of the moorings north of the New Siberian Islands or in the Beaufort Sea.

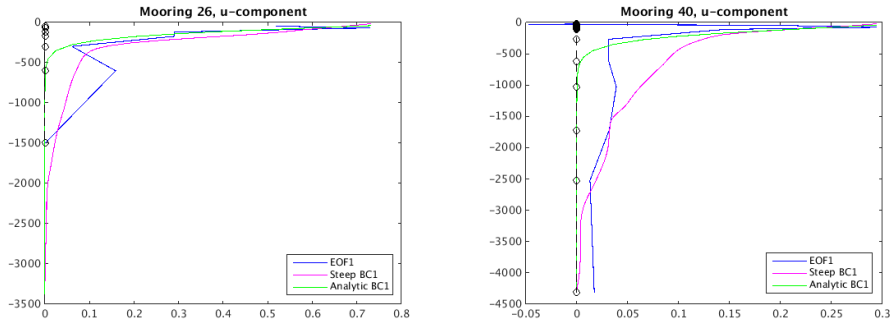

(a) Mooring 26, u component

(b) Mooring 38, u component

Figure 4.14: The dominant structure in the Arctic and the first baroclinic modal fits.

Based on the analysis from the different regions it seems like we are able to give a fairly good representation of the dominant structure using the first baroclinic mode in the mid-latitudes (northern hemisphere). If we were to say that the steep bottom modes gives a better representation of the kinetic energy partition in the ocean, we should think of the first baroclinic mode and the topographic wave as the two dominant elements. That means that we have two dominant elements that do not have to be correlated. The topographic waves are independent and advect energy off to other regions where it is likely to be dissipated by bottom drag [Ferrari & Wunsch, 2009].

4.4.2 Problematic results

When analyzing flat bottom modes we argue that the depth requirements can be relaxed as we find reasonable results when using moorings from shallower waters. For this analysis however, shallow waters have proved to be a challenge. Intuitively one could imagine that steep bottom modes would be representative in areas with a lot of topography. We find the structure in shallower waters to be too complex to be represented by one or two modes, and we do not necessarily see velocities that goes to zero at the bottom. Figure 4.15 shows two examples, both from moorings located close to the coast.

Due to numerical issues the calculations of the different modes are done on different grids. The EOFs are calculated using the measuring depths available from the respective mooring, the steep bottom modes are interpolated onto a evenly spaced grid to obtain orthogonality, and the exponential fit is done from the standard depths

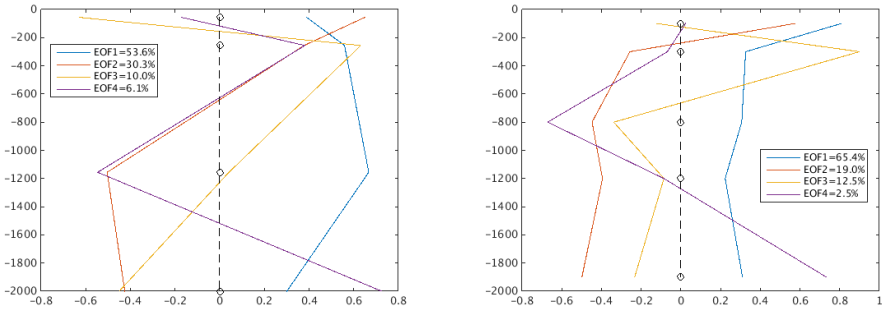

Figure 4.15: EOF 1-4 showing the complex structures of mooring 13 and 57.

provided by the climatology. This results in slight different starting depths when superimposing the modal structures onto the EOFs.

4.5 The climatology and seasonal changes

One major issues when it comes to the analysis of dynamical modes seems to be the lack of variations in the density field. The near surface structure is most influenced by seasonal changes, but also by changes over climate time scales and over shorter time periods. The depth of the mixed layer, and hence the change in upper ocean density structure, changes due to the large-scale background fields and complex inflections from eddy fields [Wunsch, 2013]. The use of an annual climatology is clearly a limitation for this study.

The annual surface temperature, salinity and potential density can be seen in figure 4.16. We see that the densest waters are found as a belt around the equator with increasing densities towards the poles. In the Arctic we see a slight decrease in surface density. This coincide well with what we see from the annual mean temperatures everywhere but in the Arctic where we see that the salinity is determining the density. The salinity in the Arctic and thereby also the density undergoes large changes with season due to ice production in winter time, and ice melt and runoff from land in summer time [Talley *et al.*, 2011]. The annual climatology is therefore a poor representation of the reality at high latitudes.

As discussed in previous sections the Brunt-Väisälä frequency, is calculated from the potential density. Figure 4.17 shows the vertical profile of the two parameters from mooring 42. The dots on the figures represents the climatology standard depths, $Z_{standard}$ for the potential density, and the mid-depths Z_{N2} for the Brunt-Väisälä frequency. We see that the Brunt-Väisälä frequency has a maximum at a depth of around 60 m.

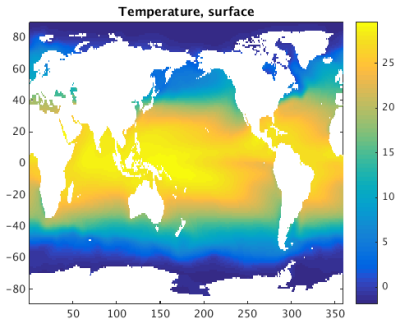

(a) Surface temperature

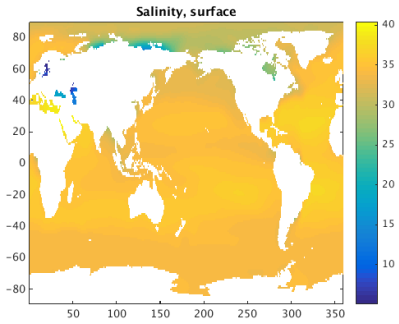

(b) Surface salinity

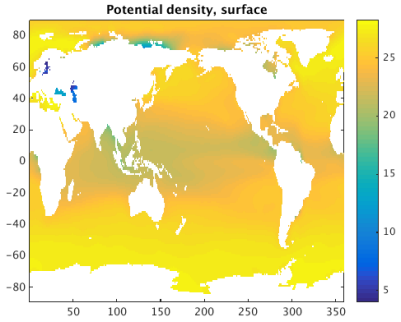

(c) Surface potential density

Figure 4.16: Annual climatology

If we look closely we see that the potential density is getting steeper in the uppermost meters. This is an indication of a surface mixed layer, where the stratification is weak, hence the decrease in N^2. We also recognize the pycnocline layer which extends down to about 1500 m, and below that the deep layer with a close to constant density. In mid-latitudes temperature is the dominant contributer to the density making the pycnocline a thermocline. Figure 4.18 shows how the temperature might change with season. Comparing the annual potential density profile to monthly profiles we see that the annual climatology tends to resemble the summer period more than the winter pe-

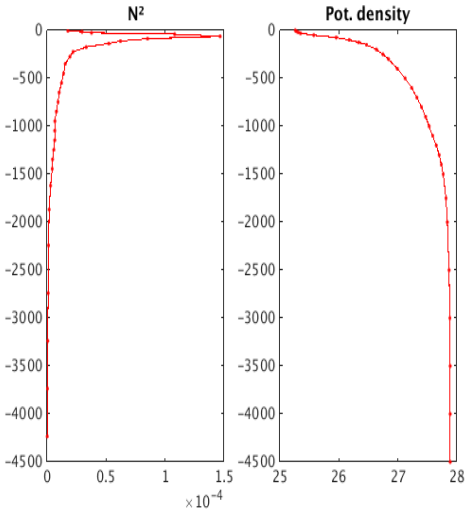

Figure 4.17: Vertical profiles of N^2 and the potential density from mooring 42.

riod. We remember that the amplitude of the modes are largest at the surface. This surface intensification is dependent upon the strength of the stratification getting more amplified with increasing stability. With a climatology that more resembles the summer stratification this could mean that the dynamical modes used in our calculations are too surface intensified to give a good representation during the winter moths.

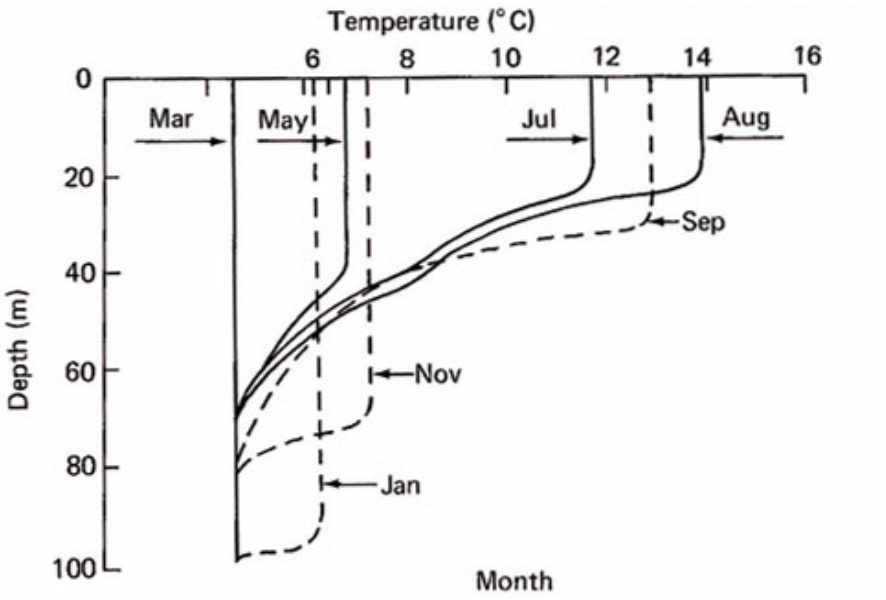

Figure 4.18: Typical changes in the thermocline with season in mid-latitudes. *Source: Talley* et al. *[2011].*

One of the features we do not capture when we use annual density fields is the change in the mixed layer depth. Figure 4.19a shows the monthly mean mixed layer depth in January and July and the maximum mixed layer depths. Figure 4.19b shows the stratification in the Labrador Sea. We see that the stratification used in this study have a very shallow mixed layer depth. This is what we would expect in summer time. We see that the maximum mixed layer depth in the area where mooring 11 and 43 are located can be as deep as 2000 m. Under such events of deep convection the flow will be barotropic in character due to the well mixed layer extending down to great depths.

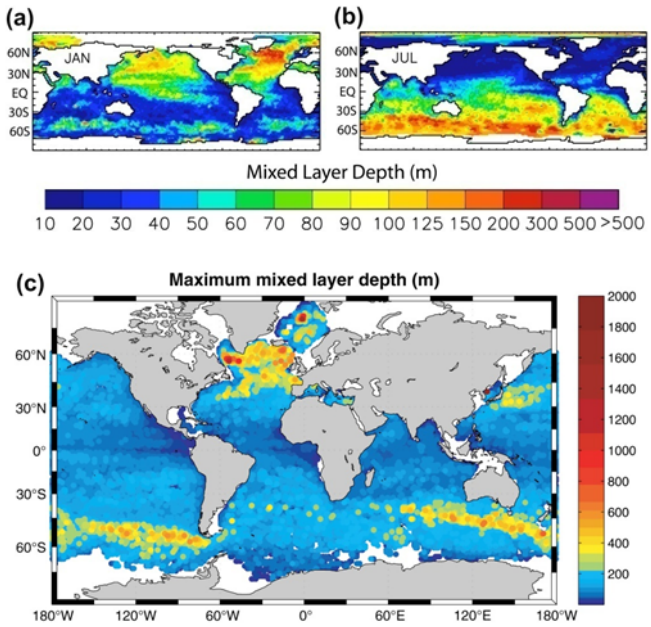

(a) The upper panel shows monthly averaged mixed layer depth in January (left) and July (right). The bottom figure shows the maximum mixed layer depth. *Source: [Talley* et al.*, 2011]*

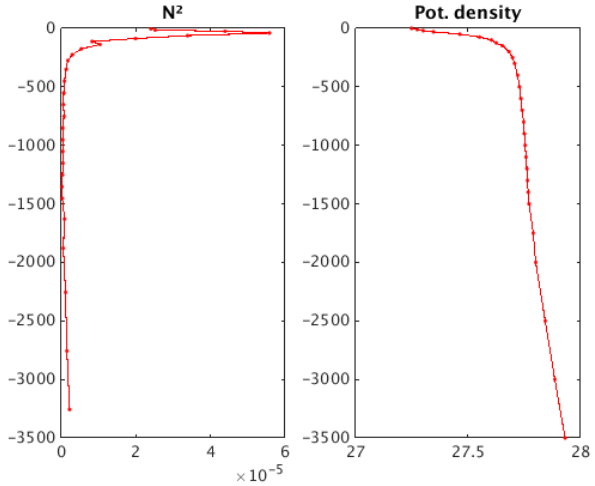

(b) Vertical profiles of N^2 and the potential density from the Labrador sea.

Chapter 5

Summary and Concluding Remarks

Since satellite data became available a couple of decades ago there has been a huge interest among oceanographers to find a way to successfully extrapolate surface motion below the surface. Being able to construct a three dimensional velocity field from altimeter data will improve our knowledge of the ocean deep circulation substantially. The work of Wunsch [1997] has remained a cornerstone in interpreting altimeter data. Under the assumption of a flat bottom ocean he found that the kinetic energy is dominated by the barotropic and first baroclinic modes, the latter one being more important in the surface layer. Hence the altimeters predominantly reflects the first baroclinic mode.

The purpose of this study was to see if the topography has any effect on the partition of energy. We introduced steep bottom dynamical mode assuming a bottom slope steep enough to have depth changes comparable to the length scale of the motion. The flow is then assumed to be zero at the bottom. A numerical scheme was constructed imposing the boundary condition of no flow at the bottom. The resulting baroclinic modes have one less zero crossing than traditional flat bottom modes. Also the barotropic mode vanishes. Instead we have a bottom trapped topographic wave which is not orthogonal to the baroclinic modes.

Observations of velocity profiles from 61 moorings are used to do a modal analysis. The vertical velocity field are decomposed into its modal components to find the relative strength of the different modes. We find the results from the flat bottom assumption to be consistent with Wunsch [1997], despite the fact that we are using different approaches for the modal fitting. For the steep bottom modes a considerable part of the motion is found to be in the topographic wave. The wave is independent of the baroclinic flow and there is no way of knowing the exact contribution from the topographic wave on the velocity profiles. Therefore we do no have a straightforward way to compare the results from the steep bottom modes to

the flat bottom modes.

EOFs were used to look at the structure only based on the statistics of the velocity fields, without making any assumptions about what the structure ought to look like. We find a dominant structure consistent with what we see in literature. On average the first EOF accounts for 75% of the variance and often resembles the first baroclinic steep bottom mode. That is a mode with no zero crossing, largest amplitude at the surface and an exponential decrease towards no flow at the bottom. We also find variability patterns that resembles a topographic wave with largest velocities at the bottom and an exponential decrease with decreasing depth.

The goal is to find a way to extrapolate the surface velocity fields below the surface. In order to do so we have to be able to predict the shape of the vertical profile of the variance. To see if the steep bottom modes are a good fit the first baroclinic steep bottom mode was superimposed onto the most dominant EOF. To have a better basis for comparison we also included an analytical solution with idealized stratification using an exponential fit found from the Brunt-Väisälä frequencies. We were able to give a fairly good representation of the structure in the pycnocline layer in the mid-latitudes. Below 1000-2000 m however, we rarely managed to capture the flow. The analytic solution seems to be the best fit everywhere except on the east coast of North America where the stratification found is deeper and the first baroclinic steep bottom mode gives the best fit. In the high latitudes, when the structure gets barotropic in character none of the modes investigated in this thesis gives a good fit. We are also struggling to capture the flow very close to the coast and in shallow areas as the structure becomes more complex and not representative by only one mode.

There are several limitations with this study. First there are large uncertainties related to observational data and the diversity of the data used for this thesis might have an influence on the quality and representativeness. We also have a poor spatial and temporal coverage making our results far from statistical significant. We have chosen to use an annual climatology to represent the density field, and the lack seasonal variation seems to be a major problem when it comes to modal fitting. This is most prominent at higher latitudes where there is large seasonal variations. The climatology seems to resemble a summer stratification more than a wither stratification which might have an effect on our results.

Further investigation has to be done to conclude if the steep bottom modes give a better representation of the energy partition than the flat bottom modes. A continuation of the present work would be to figure out what is causing the different results between i.e. the Atlantic Ocean and the Pacific. It would also be useful to extend the coverage and to look at monthly or *in situ* stratification rather than annual averages. To relate this study to the extrapolation of surface velocities further investigation into the prediction of the shape of the vertical structure has to be

done. It would also be of interest to investigate how topographic waves are interacting with baroclinic modes and what effect it has on the energy partition.

The question posed in the motivation on whether the most dominant EOF should be interpreted as a coupling between the barotropic and first baroclinic mode remain unanswered. We have however shown that there is reason to further investigation on the importance of the steep barotropic mode as the most dominant element together with the topographic wave. If this turns out to be true we only need to interpret the altimeter data as a single mode which is a substantial improvement as opposed to the two dominant modes found by Wunsch. Also the difficulties around the coupling between two dominant modes are avoided if the steep bottom modes proves to be most representative. The topographic wave is independent of the barotropic modes and the two domination elements does not have to be correlated. The energy can then be advected off to other regions by the topographic wave, where it is likely to be dissipated from bottom drag.

Appendix A

Table 5.1: Information about the moorings analyzed; latitude, longitude, percentage of mean kinetic energy in the baroclinic and first barotropic modes of the u and v component, sea floor depth and the deepest measuring depth (Deepest), duration (D), number of instruments (M), instrument type and the source.

No	Latitude	Longitude	BT_u	BC1_u	BT_v	BC1_v	Sfdepth	Deepest	D	M	Instrument type	Source
1	32,7010	231,9380	53,8	33,9	57,3	29,4	4524	1481	388	4	Aanderaa RCM5	OSU disk 1
2	32,1550	231,9920	60,2	14,6	52,1	23,5	4280	1419	386	4	Aanderaa RCM5	OSU disk 1
3	45,4560	228,8230	32,5	42,7	34,6	38,4	2836	2500	396	6	Aanderaa RCM	OSU disk 1
4	-37,6700	167,2700	48,6	32,7	46,7	31,8	1014	1004	220	4	Aanderaa RCM4/5	OSU disk 1
5	34,0370	289,9570	60,2	33,1	54,2	32,3	5366	4000	335	10	VMCM&VACM	OSU disk 1
6	33,9770	289,9930	71,6	22,9	44,7	44,4	5366	4000	234	14	VACM	OSU disk 1
7	26,4890	283,5520	48,0	26,1	61,5	21,6	4850	3800	569	5	VACM	OSU disk 1
8	26,4750	283,8980	43,0	38,6	38,7	44,1	4810	3800	285	6	VACM&RCM	OSU disk 1
9	11,3800	53,0100	48,1	41,3	33,3	46,6	700	645	573	6	RCM8	OSU disk 1
10	10,2000	53,6300	15,4	46,9	28,6	32,3	4305	4230	569	7	RCM8	OSU disk 1
11	56,7530	307,5450	74,4	10,8	82,7	8,0	3510	3476	381	6	RCM8	OSU disk 1
12	-34,5430	333,0250	29,8	36,9	25,0	37,6	4325	4310	486	21	ADCP&RCM8	OSU disk 1
13	42,2670	349,8500	54,3	22,5	55,6	25,2	2700	2000	341	4	RCM4s&RCM7	OSU disk 1
14	26,4980	284,3170	55,9	30,2	44,2	41,2	4689	4000	757	6	VACM	OSU disk 1
15	26,4870	288,8330	43,7	12,1	49,3	13,0	5488	4000	376	7	VACM & Aanderaa RCM	OSU disk 1
16	26,5000	283,9000	57,1	26,8	54,5	25,5	4807	4000	596	7	VACM & Aanderaa RCM	OSU disk 1
17	41,9720	207,9930	40,0	27,2	38,9	24,6	5150	3756	355	7	not available	OSU disk 1
18	27,9980	208,0520	36,8	34,3	37,7	40,0	5300	3919	369	10	not available	OSU disk 1
19	41,9900	207,9450	30,2	28,1	24,3	28,0	5150	3980	301	10	not available	OSU disk 1
20	28,0330	207,9000	11,3	50,2	30,2	47,6	5300	3984	296	10	not available	OSU disk 1
21	-11,2670	122,9170	39,6	14,0	28,4	21,3	1895	1400	349	26	ADCP	OSU disk 1
22	-11,4170	122,9830	29,5	24,6	26,2	24,8	1197	870	416	26	ADCP	OSU disk 1
23	47,4230	220,7030	25,7	16,3	29,1	16,0	4224	3999	311	14	VMCM&RCM5	OSU disk 1
24	73,3860	359,1720	30,4	32,3	24,1	28,9	3131	2472	318	8	ADCP	OSU disk 2
25	72,6200	216,4320	11,0	43,2	23,9	29,8	3339	1534	488	7	Aanderaa RCM	OSU disk 2
26	72,5420	216,1700	13,1	38,0	15,0	34,6	3370	1500	344	7	Aanderaa RCM	OSU disk 2
27	78,5130	133,9620	64,0	13,8	62,8	14,1	1761	1161	384	4	RCM/8	OSU disk 2
28	81,0750	138,9000	52,1	13,7	52,5	17,5	1712	1692	367	5	RCM7/8	OSU disk 2
29	80,3200	150,0570	66,3	16,0	47,2	22,1	1699	1109	367	4	RCM7/8	OSU disk 2
30	75,4980	348,8780	56,6	26,0	45,4	33,5	1312	1307	365	4	Neil Brown ACM-2/Aanderaa RCM	OSU disk 2
31	75,0780	347,8470	58,1	26,6	47,4	35,2	1263	1242	365	4	Neil Brown ACM-2/Aanderaa RCM	OSU disk 2
32	74,9930	350,8980	66,9	16,1	64,7	12,3	3317	3253	178	4	Aanderaa RCM	OSU disk 2
33	74,9710	348,4160	63,5	30,0	60,7	31,0	2300	2188	436	4	Aanderaa RCM	OSU disk 2
34	74,9930	349,3920	71,0	21,4	74,1	19,0	3075	2971	410	4	Aanderaa RCM	OSU disk 2
35	-72,5570	339,4050	35,3	28,8	40,8	41,8	3415	3411	129	8	Aanderaa RCM	OSU disk 2
36	89,4550	54,3290	58,7	7,9	56,3	9,3	4295	2508	361	25	ADCP	OSU other
37	89,2530	64,6920	46,1	21,4	49,0	19,4	4345	4336	364	25	not available	OSU other
38	89,3470	77,1200	50,3	8,0	43,5	10,3	4315	4306	719	29	not available	OSU other
39	25,8720	265,1200	52,2	40,1	37,7	55,4	3000	1500	110	4	not available	OSU other
40	25,4920	265,8400	49,5	41,9	52,6	39,0	3500	3000	129	5	not available	OSU other
41	73,8290	355,1660	73,7	21,6	63,2	28,6	3570	1503	421	4	not available	OSU other
42	21,2166	335,5767	52,1	26,5	52,3	31,3	4960	4920	277	5	not available	Wunsch1997
43	56,9567	308,4117	82,3	8,8	73,4	13,2	3560	3545	143	5	not available	Wunsch1997
44	57,1150	350,6367	63,5	27,0	63,6	25,8	992	892	118	4	not available	Wunsch1997
45	41,9717	207,9933	39,9	27,2	38,9	24,6	5150	3756	355	7	not available	NODC F015
46	27,9983	208,0517	36,8	34,2	37,7	40,0	5300	3919	369	10	not available	NODC F015
47	41,9900	207,9450	30,3	28,1	24,3	28,0	5150	3980	301	10	not available	NODC F015
48	28,0333	207,9000	10,8	52,9	36,0	44,2	5300	3984	296	10	not available	NODC F015
49	55,4057	203,6668	49,9	25,5	63,0	17,9	190	172	295	6	not available	NODC F015
50	55,3688	204,9375	57,5	29,7	48,7	28,8	1189	1000	295	7	not available	NODC F015
51	25,4917	265,8400	49,4	41,9	52,6	39,1	3500	3000	129	5	not available	NODC F015
52	55,9571	203,6227	58,3	32,2	53,5	35,0	227	202	331	4	not available	NODC F015
53	45,4563	228,8227	32,5	42,8	34,6	38,6	2836	2506	396	6	not available	NODC F015
54	73,8287	355,1663	73,7	21,6	63,2	28,6	3570	1503	421	4	not available	NODC F015
55	36,3050	286,2718	41,3	35,1	33,9	42,6	3006	1200	178	4	not available	NODC F015
56	36,2517	285,6733	32,9	48,4	45,1	38,2	2020	1900	211	5	not available	NODC F015
57	36,2517	285,6733	26,2	33,6	55,6	22,6	2020	1900	118	5	not available	NODC F015
58	36,2517	285,6733	39,8	27,5	49,1	28,2	2020	1900	168	5	not available	NODC F015
59	37,5842	4,4983	68,8	21,9	55,3	31,4	2738	2000	281	4	not available	IFREMER
60	-33,9850	114,4150	58,2	23,1	69,4	20,5	720	320	168	4	Aanderaa RCM8	CSIRO
61	-23,3067	48,5700	12,9	42,7	47,3	26,8	3580	2983	314	5	AACM/NWCM/VACM	Zantopp

Bibliography

Antonov, John I., Seidov, Dan, Boyer, Timothy P., Locarnini, Ricardo A., Mishonov, Alexey V., Garcia, Hernan E., Baranova, Olga K., Zweng, Melissa M., & Johnson, Daphne R. 2010. *World Ocean Atlas 2009, Volume 2: Salinity*. Tech. rept.

Beardsley, R. C. 1987. A comparison of the vector-averaging current meter and new Edgerton, Germeshausen, and Grier, Inc., vector-measuring current meter on a surface mooring in Coastal Ocean Dynamics Experiment 1. *Journal of Geophysical Research*, **92**(C2), 1845.

Bjornsson, H, & Venegas, SA. 1997. *A manual for EOF and SVD analyses of Climate Data*. Tech. rept.

Cabanes, C, Huck, T, Verdière, a Colin De, Ollitrault, M, & Gaillard, F. 2008. Partition Between Barotropic And First First Baroclinic Modes from Altimetric Velocities and Argo Float Float Mid-depth Displacements. **4**(4), 4190.

Chelton, Dudley B., Schlax, Michael G., & Samelson, Roger M. 2011. Global observations of nonlinear mesoscale eddies. *Progress in Oceanography*, **91**(2), 167–216.

De Mey, Pierre, & Robinson, Allan R. 1987. Assimilation of Altimeter Eddy Fields in a Limited-Area Quasi-Geostrophic Model. *Journal of Physical Oceanography*, **17**(12), 2280–2293.

Dickson, R. R. 1983. *"Global summaries and intercomparisons: flow statistics from long-term current meter moorings." Eddies in Marine Science*. Springer-Verlag.

Emery, William J, & Thomson, Richard E. 1998. *Data Analysis Methods in Physical Oceanography*. Vol. 22. Elsevier.

Ferrari, Raffaele, & Wunsch, Carl. 2009. *Ocean Circulation Kinetic Energy: Reservoirs, Sources, and Sinks*.

Guinehut, Stephanie, Le Traon, Pierre Yves, & Larnicol, Gilles. 2006. What can we learn from Global Altimetry/Hydrography comparisons? *Geophysical Research Letters*, **33**(10).

Joseph, Antony. 2014. *Measuring Ocean Currents*. 1st edn. Elsevier.

Kundu, Pijush K., Allen, J. S., & Smith, Robert L. 1975. *Modal Decomposition of the Velocity Field near the Oregon Coast*.

LaCasce, J. H. 2012. *Surface Quasigeostrophic Solutions and Baroclinic Modes with Exponential Stratification*.

LaCasce, J. H. 2014. *Atmosphere-Ocean Dynamics*. Tech. rept.

LaCasce, J. H., & Mahadevan, A. 2006. Estimating subsurface horizontal and vertical velocities from sea-surface temperature. *Journal of Marine Research*, **64**(5), 695–721.

LaCasce, J. H., & Wang, Jinbo. 2015. Estimating subsurface velocities from surface fields with idealized stratification. *Journal of Physical Oceanography (in press)*.

Lapeyre, G., & Klein, P. 2006. Dynamics of the Upper Oceanic Layers in Terms of Surface Quasigeostrophy Theory. *Journal of Physical Oceanography*, **36**(2), 165–176.

Lay, David C. 2012. *Linear Algebra and Its Applications*. 4th edn. Pearson.

Locarnini, R. A., Mishonov, A. V., Antonov, J. I., Boyer, T. P, Garcia, H. E., Baranova, O. K., Zweng, M. M, & Johnson, R. D. 2010. *World Ocean Atlas 2009, Volume1: Temperature*. Tech. rept.

Müller, T.˜J., & Siedler, G. 1992. Multi-year current time series in the eastern North Atlantic ocean. *J. Mar. Res.*, **50**(1), 63–98.

NASA. *Ocean Surface Topography From Space*.

NOAA. *Data Sets & Products, World Ocean Atlas 2009*.

Pedlosky, Joseph. 1979. *Geophysical Fluid Dynamics*. Springer-Verlag.

Samelson, R. M. 1992. Surface-intensified Rossby waves over rough topography. *Journal of Marine Research*, **50**(3), 367–384.

Scott, Robert B., & Arbic, Brian K. 2007. Spectral Energy Fluxes in Geostrophic Turbulence: Implications for Ocean Energetics. *Journal of Physical Oceanography*, **37**(3), 673–688.

Scott, Robert B., & Furnival, Darran G. 2012. Assessment of Traditional and New Eigenfunction Bases Applied to Extrapolation of Surface Geostrophic Current Time Series to Below the Surface in an Idealized Primitive Equation Simulation. 165–178.

Scott, Robert B, & Furnival, Darran G. 2013. A guide to GMACMD. 1–55.

Smith, K. Shafer. 2007. The geography of linear baroclinic instability in Earth's oceans. *Journal of Marine Research*, **65**(5), 655–683.

Smith, K. Shafer, & Vallis, Geoffrey K. 2001. The Scales and Equilibration of Midocean Eddies: Freely Evolving Flow. *Journal of Physical Oceanography*, **31**.

Sprintall, & Cronin, M F. 2001. Upper Ocean Vertical Structure. *Eos*, 1–9.

Stommel, Henry. 1948. The westward intensification of wind-driven ocean currents. *Trans. Amer. Geophys. Union*, **29**(2), 202–206.

Sverdrup, H U. 1947. Wind-Driven Currents in a Baroclinic Ocean; with Application to the Equatorial Currents of the Eastern Pacific. *Proceedings of the National Academy of Sciences of the United States of America*, **33**(11), 318–326.

Talley, Lynne, Pickard, George, Emery, William J, & Swift, James. 2011. *Descriptive Physical Oceanography. An Introduction*. 6th edn. Elsevier.

Vallis, Geoffrey K. 2006. Atmospheric and oceanic fluid dynamics: fundamentals and large-scale circulation. *Cambridge University Press*, 745.

Wang, Jinbo, Flierl, Glenn R, LaCasce, J. H., McClean, Julie L., & Mahadevan, A. 2013. Reconstructing the Ocean's Interior from Surface Data.

Weisstein, Eric W. *Bessel Function*.

Weller, Robert A., & Davis, Russ E. 1980. A vector measuring current meter. *Deep Sea Research Part A. Oceanographic Research Papers*, **27**(7), 565–581.

Wunsch, Carl. 1997. The Vertical Partition of Oceanic Horizontal Kinetic Energy. *Journal of Physical Oceanography*, **27**(8), 1770–1794.

Wunsch, Carl. 2013. Baroclinic motions and energetics as measured by altimeters. *Journal of Atmospheric and Oceanic Technology*, **30**(1), 140–150.

Wunsch, Carl, & Stammer, Detlef. 1997. Atmospheric loading and the oceanic inverted barometer effect. *Reviews of Geophysics*, **35**(1), 79.